Palaeogeography, Palaeoclimatology, Palaeoecology 637 (2024) 112019

Contents lists available at ScienceDirect

Palaeogeography, Palaeoclimatology, Palaeoecology

journal homepage: www.elsevier.com/locate/palaeo

Extremely high resolution XRF core scanning reveals the Early Triassic depositional history of the Montney Formation in northeastern British Columbia, Canada

Shane D. Schoepfer [a,*], Charles M. Henderson [b], Thomas F. Moslow [b,c], Chen Shen [d]

[a] Department of Geosciences and Natural Resource, Western Carolina University, Cullowhee, NC 28723, USA
[b] Department of Earth, Energy and Environment, University of Calgary, Calgary, AB T2N 1N4, Canada
[c] Moslow Geoscience Consulting Ltd., Calgary, AB T3L 1W9, Canada
[d] CNOOC Research Institute Ltd., Beijing 100028, China

ARTICLE INFO

Editor: L Angiolini

Keywords:
ITRAX
Geochemistry
Principal components analysis
Mass extinction recovery
Slide Mountain Ocean
Yukon-Tanana Terrane

ABSTRACT

The Montney Formation is a laterally extensive, fine-grained sedimentary unit in western Alberta and northeastern British Columbia, and a major target of hydrocarbon exploration. It also retains a complete record of the Early Triassic epoch, a time when the biosphere was recovering from the effects of the end-Permian mass extinction. An industry well provides a full-diameter core of the complete distal Montney Formation in northeastern British Columbia (over 350 m thick), with stratigraphic age control provided by conodont biostratigraphy and regional correlations. For this study, the core was scanned using an ITRAX X-ray fluorescence spectrometer, at centimeter-scale resolution. The resulting dataset (over 37,000 individual measurements) provides an extremely high level of resolution for a deep-time geochemical study. While the data generated by this instrument are semiquantitative, they can be calibrated by correlating them with more conventional ICP-MS and XRF measurements of select samples. Using this method, we assessed the reliability of each of the elemental data series, and where possible converted them to quantitative geochemical measurements. These calibrated measurements serve as the basis for our detailed reconstruction of the Montney Formation's depositional history.

The distal Montney depositional basin, including the location of the c-65-F core, was euxinic immediately following the end-Permian mass extinction, and accumulated sediments from the rapidly eroding margin of western North America. Conditions stabilized somewhat in the Dienerian, with oxic bottom water and a trend toward more compositionally mature sediment, but conditions of widespread euxinia and rapid erosion of the North American craton recurred in the early Smithian, earlier than this global crisis has been recognized elsewhere. Above the middle-upper Montney sequence boundary, in the overlying Spathian succession, local effects predominate. Coastal upwelling resumed in the basal Spathian, though the Montney depositional basin was soon cut off from the global ocean by uplift of the Yukon-Tanana arc bounding the basin to the west. Restricted conditions, with euxinic bottom water, were punctuated by oxic intervals, when rising sea level allowed the basin to freely exchange water with the open ocean. Intervals of restriction became progressively less acute in the upper Spathian.

1. Introduction

The Montney Formation is a laterally extensive, fine-grained Lower Triassic sedimentary unit underlying parts of western Alberta and northeastern British Columbia, Canada. The unit is as much as 400 m thick even in distal environments, and has major potential as a tight gas formation. It is estimated to contain over 449 trillion cubic feet of recoverable natural gas and over 14.5 billion barrels of natural gas liquids, making it a promising target for hydrocarbon development (National Energy Board, 2013). Spanning the entirety of the Early Triassic, it also provides a valuable record of greenhouse warming, extinction, and biotic recovery.

The Montney Formation was deposited on a remnant of the cratonic margin and in the Slide Mountain Ocean, which originated as an

* Corresponding author.
E-mail address: sschoepfer@wcu.edu (S.D. Schoepfer).

https://doi.org/10.1016/j.palaeo.2024.112019
Received 23 August 2023; Received in revised form 29 December 2023; Accepted 3 January 2024
Available online 4 January 2024

extensional back-arc basin during the late Paleozoic (Rohais et al., 2018). This seaway was bounded to the east by the western coast of Pangaea, and to the west by the Yukon-Tanana arc, and it may have received sediments from both of these subaerially exposed landmasses. The Yukon-Tanana complex accreted to western North America during the Late Permian (260–252.5 Ma), associated with rapid closure of the Slide Mountain Ocean. This accretion event is recognized as the Sonoma Orogeny in the southwestern United States and as the Klondike Orogeny in western Canada (Beranek and Mortensen, 2011). By the earliest Triassic, the remaining Slide Mountain Ocean likely existed as a narrow seaway running through a foreland-type basin, which may have experienced restricted communication with the broader Panthalassic Ocean (Schoepfer and Henderson, 2022).

As the Slide Mountain Ocean was closing, the global ocean was experiencing the prolonged aftermath of the end-Permian mass extinction, the most severe biodiversity crisis of the Phanerozoic. Rapid warming of the oceans and atmosphere (Sun et al., 2012), associated with the emplacement of the Siberian Traps, led to a series of marine environmental stresses including widespread ocean anoxia and euxinia (Zhang et al., 2018a), acidification (Song et al., 2021), rapid influx of terrigenous sediment (Algeo and Twitchett, 2010), disruption of the marine nitrogen cycle (Grasby et al., 2016), and reduced upwelling along western Pangaea (Schoepfer et al., 2013). Rates of biotic recovery varied regionally during the Early Triassic, but full recovery took approximately 5 million years, and was interrupted by repeated environmental stresses, including a second episode of intense warming in the Smithian (Wei et al., 2015; Zhang et al., 2019a, 2019b).

The combination of evolving climatic and oceanographic conditions and biological responses in a tectonically dynamic environment makes reconstruction of the Montney depositional system challenging. Conventional geochemical approaches can be used to reconstruct local changes in redox conditions and primary productivity (Algeo and Liu, 2020), but would have difficulty deconvolving the effects of changing sediment provenance, basinal restriction, and real, possibly global ocean chemistry change over time. To address these questions, we studied a unique, extremely high-resolution (XHR) X-ray fluorescence record of the complete distal Montney Formation from northeastern British Columbia.

With 30 elements measured at over 37,000 horizons by an ITRAX core scanner (Croudace et al., 2006), our dataset includes >1.1 million individual geochemical measurements at centimeter scale resolution. Sedimentation rates constrained by biostratigraphy (Moslow et al., 2018) suggest that each 1 cm horizon represents, on average, approximately 100 years, a level of stratigraphic resolution unprecedented in studies of the Lower Triassic globally. The richness of the dataset makes it a valuable resource for exploratory data analysis techniques such as principal components analysis (Shaw, 2009), while the degree of detail allows for a reconstruction of the evolution of the depositional basin, and the recognition of key biological and sequence stratigraphic horizons. This study illustrates the potential of XHR geochemical datasets and serves as a model for future XHR studies of specific sedimentary units.

2. Geologic setting

2.1. The Slide Mountain Ocean

The Slide Mountain Ocean originated as a back-arc extensional basin

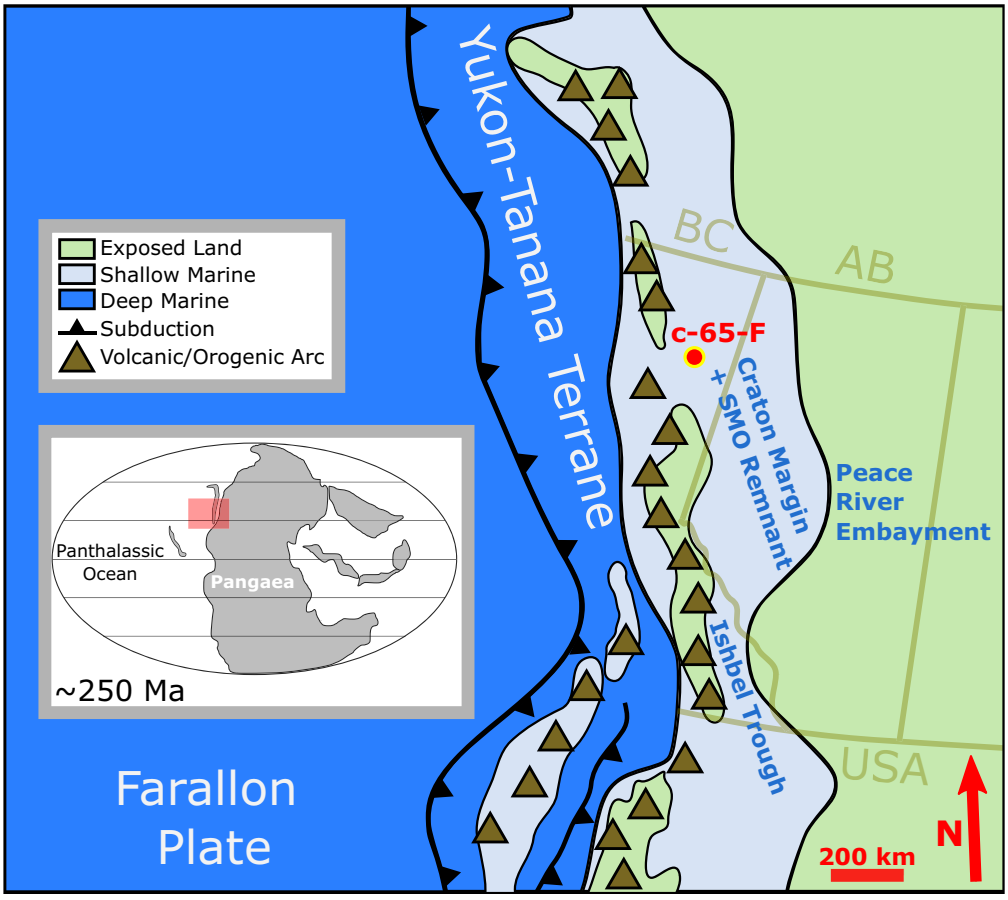

Fig. 1. Paleomap of western Canada during the Early Triassic (~250 Ma), showing the depositional location of Core c-65-F, in the remnant Slide Mountain Ocean inboard of the Yukon-Tanana arc. Inset at bottom left shows the location of the paleomap on the subtropical western margin of Pangaea (Nelson et al., 2006; Colpron and Nelson, 2009; Beranek et al., 2010; Beranek and Mortensen, 2011; Rohais et al., 2018; Schoepfer and Henderson, 2022).

along the western margin of Pangaea. The seaway was bound to the east by the downwarped margin of the North American continent, and to the west by the composite Yukon-Tanana arc, which comprises the Stikine, Quesnel, and Yukon-Tanana terranes (Fig. 1; Nelson et al., 2006). The Slide Mountain Ocean may have reached widths of as much as 1200 to 2400 km by the Middle Permian (Beranek and Mortensen, 2011; Colpron and Nelson, 2009), and likely experienced western-boundary coastal upwelling leading to widespread deposition of siliceous biogenic sediments and phosphatogenesis (Beauchamp and Baud, 2002; Beauchamp and Grasby, 2012; Schoepfer et al., 2013).

By the Late Permian the Slide Mountain Ocean was closing rapidly, and had become a narrow, approximately linear seaway (Zonneveld and Moslow, 2018). Accretion of the offshore terranes to continental North America continued throughout the Late Permian (Beranek and Mortensen, 2011), and by the Early Triassic the Slide Mountain Ocean may have been only poorly connected with the broader Panthalassic realm (Schoepfer and Henderson, 2022). Despite this intermittent connection with the Panthalassic realm, the basin likely retained fully marine (euhaline) salinities during deposition, consistent with its position on the arid, subtropical margin of Pangaea (Davies et al., 1997, 2018). A full discussion of geochemical evidence for salinity can be found in the Supplementary Text and Fig. S1.

The Slide Mountain Ocean experienced a rapid transition from biogenic to siliciclastic sediment deposition across the Permian-Triassic boundary, reflecting both the extinction of the silica-producing sponge fauna and the accelerated erosion of adjacent landmasses, with a major increase in sedimentation rate (Wignall and Newton, 2003; Algeo and Twitchett, 2010). The Montney Formation was deposited during this interval of rapid erosion, and mainly comprises angular, mineralogically immature siltstone and very fine sandstone, as well as *Claraia* biostromes, minor phosphatic intervals, and discrete dolostone beds (Zonneveld et al., 2010; Moslow et al., 2018).

2.2. Core c-65-F

Core c-65-F was recovered from a site approximately 20 km north of Hudson's Hope, British Columbia and roughly 5 km to the east of the northern Rocky Mountain deformation front (c-65-F/94-B-8, Dominion Land Survey grid system), representing the more distal depositional facies of the Montney Formation. This core is one of many in this region, and regional cross-sections supported by biostratigraphy (Henderson et al., 2018) demonstrate a complete and uninterrupted succession in c-65-F. The studied interval of 7.5 cm-diameter core spans 395 m of continuous strata, including the uppermost Permian Belloy Formation, the entire Lower Triassic Montney Formation, the Sunset Prairie Formation, and lowermost Phosphate Member of the Middle Triassic Doig Formation (Zonneveld and Moslow, 2018). The interval recovered was from 2185 – 2580 meters below the surface (mbs).

A distinct coplanar sequence boundary/flooding surface at ~2374 mbs divides the Lower Triassic succession into informal "Middle Montney" and "Upper Montney" units. Conodont biostratigraphy (Moslow et al., 2018; Henderson et al., 2018) indicates that this surface represents a conformable sub-Spathian boundary. The sub-Smithian sequence boundary (2504 mbs, separating the informal "Lower Montney" and "Middle Montney" units) is a correlative conformity, equivalent to the sharp unconformity recognized in more proximal depositional settings to the east. The locations of the Griesbachian/Dienerian and Dienerian/Smithian boundaries, as shown in Figs. 4–6, have been revised from those in Moslow et al. (2018), based on unpublished conodont biostratigraphy from core material of equivalent age and regional subsurface correlations (Henderson et al., 2018). A complete description of the core can be found in the Supplementary Text.

2.3. Biostratigraphy of the Montney Formation

Henderson et al. (2018) summarized the conodont biostratigraphy for the Montney Formation and provided tables for the known productive samples at the time, including the c-65-F/94-B-8 core discussed in this paper. Fig. S2 (modified from Moslow et al., 2018) shows the distribution of taxa in c-65-F which were recovered from a number of core slabs. While some key taxa were recovered, overall the conodonts were sparse, largely related to the difficulty of breaking down these siltstone rocks. Subsequently, a new core was studied by Brar (2021) from the 6–3-79-13W6 well. In this case, a slab of this 314 m continuous core was crushed into pseudo-cuttings or chips, approximately 2–3 mm in size, with every meter sampled. Recovery from these pseudo-chip samples was extraordinary – in many cases the conodonts were physically disaggregated from the matrix, either fragmented or whole (see plates in Brar, 2021). The detailed biostratigraphic framework from 6–3-79-13W6 has been correlated to the c-65-F/94-B-8 core using regional wireline log correlation as well as the detailed sedimentology and identified flooding surfaces (Fig. S2). The result of this correlation is the recognition of 15 biozonal intervals that constrain the relative ages of the succession shown in the various figures. These zonal intervals are described more fully in the Supplementary Text.

3. Methods

3.1. ITRAX ED-XRF core scanning

An interval of core c-65-F ranging from 2181.00 – 2576.35 mbs was cut lengthwise to produce a flat surface, and analyzed with an ITRAX core scanner (see Croudace et al., 2006), an automated X-ray fluorescence analyzer, at the Institut National de la Recherche Scientifique, Québec City, generally at centimeter resolution (Fig. 2). Full details on the core scanning procedure are given in the Supplementary Text.

The values generated by ITRAX core scanning are not direct measurements of elemental concentration (Croudace et al., 2006). The measurements, reported in counts per second (cps) of emitted X-rays, would ideally have a linear relationship with concentration, however this may be modified by the energy of various emitted X-rays, interferences by elements with similar X-ray energies, and matrix effects resulting from the variable composition of the core (Thomson et al., 2006; Löwemark et al., 2019).

To calibrate the dataset, 23 powdered samples from core c-65-F were sent to ALS Chemex for geochemical analysis via inductively coupled plasma mass spectroscopy (ICP-MS). This method measured 25 of the 30 elements reported in the ITRAX data (excluding Si, Cl, Sm, Yb and Po). Since the digestion method used in this technique removes silica, silicon was measured in the same samples using a Niton XL3t handheld X-ray fluorescence spectrometer. Details of these measurements are given in the Supplementary Text. The correlation between ITRAX cps measurements and conventional geochemical data was variable. The ranges of both the uncalibrated and calibrated datasets are reported in Table 1, which also includes the correlation coefficients and error associated with the calibration. Each element was assigned a calibration quality rating of Good, Fair, or Poor, with only those elements rated Good being used for interpretation of the depositional environment, and only those rated Good or Fair used for Principal Components Analysis. See the Supplementary Text for a more detailed discussion of the calibration procedure.

3.2. Principal components analysis

Principal components analysis (PCA) is an exploratory data reduction technique that seeks to reduce complex datasets to a limited number of components (Shaw, 2009). Each principal component (PC) is correlated, positively or negatively, with each of the elements in the dataset. PCA was run on the calibrated dataset (including only those elements with a 'Good' or 'Fair' calibration rating) using PAST 4.01 data analysis software (Hammer et al., 2001). Due to the inclusion of both major and trace elements, the analysis was run on a correlation matrix, which

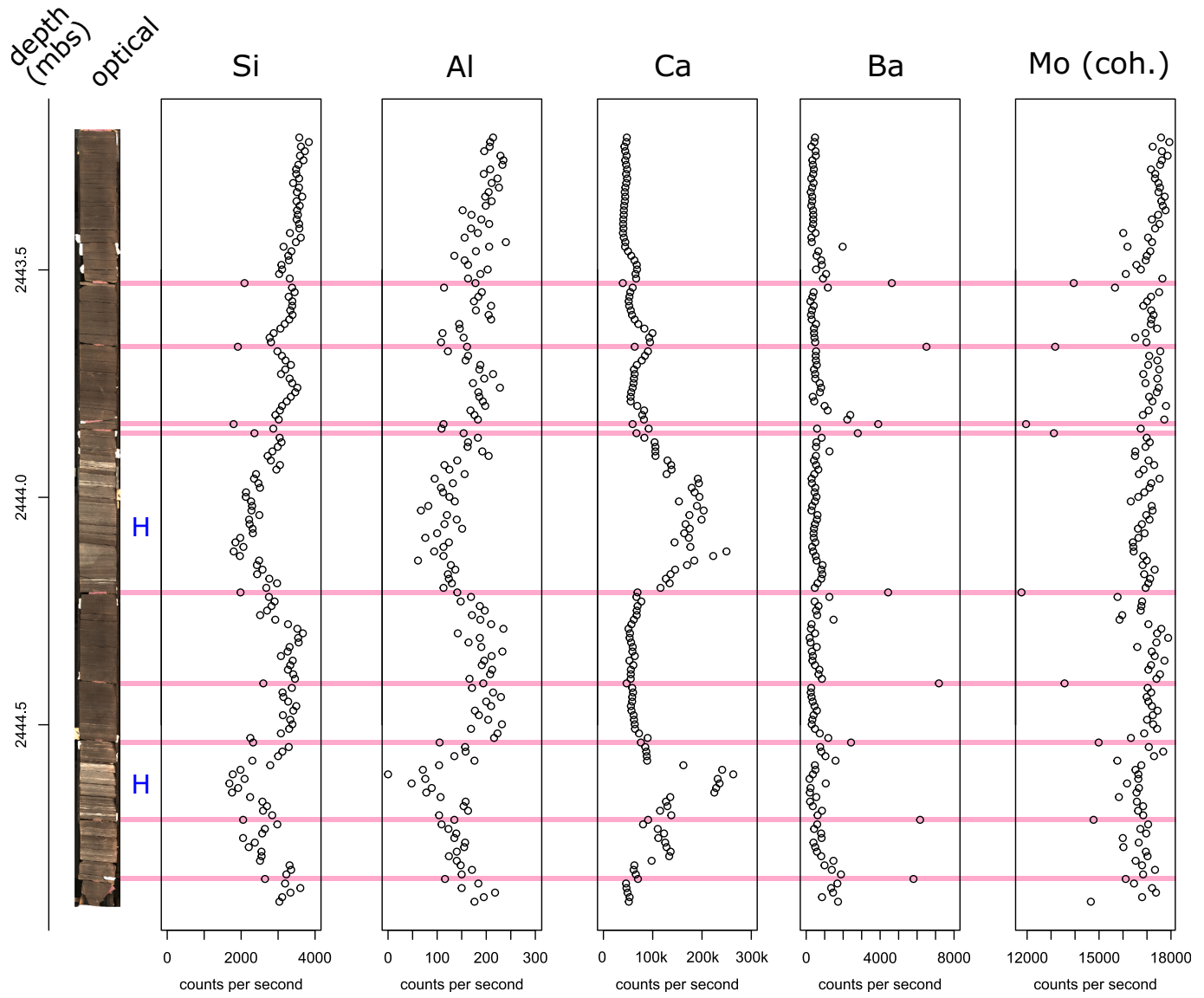

Fig. 2. Optical scan of a core section with correlative XRF geochemical measurements. The chosen example is typical of mid-Smithian strata, and shows two hemipelagic calcispheric dolosiltstone intervals (lighter colored beds; labeled 'H), corresponding with decreased Si and Al measurements and elevated Ca measurements. Pink highlights show locations of foam polymer filler (see Supplementary Text), which can be readily identified in the optical scan as well as via elevated Ba values and decreased coherent scattering of Mo X-rays. These points were removed from the compiled dataset. In depth scale, mbs refers to meters below surface. (For interpretation of the references to color in this figure legend, the reader is referred to the web version of this article.)

weights all elements equally regardless of their absolute value in cps, ensuring that the principal components are not dominated by the most abundant major elements.

By examining the positive and negative correlations of each principal component (PC) with various elements (loadings), and considering the known geochemical behaviors of those elements, we can interpret each PC in light of a probable depositional signal that it predominantly represents. The scores of each PC can also be plotted for each individual sample in the compiled dataset, allowing us to examine stratigraphic variation.

4. Results

The calibrated dataset consists of a total of 37,127 measured horizons, spanning the uppermost Belloy Formation, the entirety of the Montney Formation, the Sunset Prairie Formation, and the lower Doig Formation in Core c-65-F. Calibrated values of 26 elements were determined for each horizon (Al, As, Ba, Ca, Ce, Cr, Cu, Fe, Ga, K, Mn, Ni, P, Pb, Rb, S, Si, Sr, Ta, Th, Ti, U, V, Y, Zn, Zr). The full calibrated dataset is available in the Supplement (Table S1). Summary statistics for each element by formation and substage are provided in Table 2.

4.1. Major element geochemistry

Calibrated measurements of major element chemistry generally track observed lithologic changes in core c-65-F (Fig. 4). Silicon decreases significantly at the contact between the cherty Belloy Formation (mean = 37.29%, s.d. = 3.93%) and the overlying Montney Formation (mean = 28.10%, s.d. = 4.10%). Si is generally fairly consistent through the Montney, but does reach values above 35% in the lower Spathian, coincident with changes in provenance indicators (see below). The sandy Sunset Prairie Formation shows higher values than the Montney (mean = 30.35%, s.d. = 3.93%), while the Doig Formation shows substantially lower values (mean = 19.70%, s.d. = 3.68%).

Calcium content generally reflects carbonate content in the sediment, with positive Ca excursions corresponding to observed calcisphere

Table 1
Summary statistics for all 30 elements measured by XRF core scanning, showing percentile values for raw counts per second, parameters for calibrating counts per second, and summary statistics of the calibrated dataset. s.d. = standard deviation, n = the number of handheld XRF or ICP-MS measurements used for calibration, RMSE = root mean squared error, RMS %err = root mean squared percent error.

	Raw ITRAX data (counts per second)							Calibration parameters								Calibrated Dataset						
	Percentile					Mean	s.d.	Method	Unit	ITRAX pts	n=	r^2	RMSE	RMS %err	Calibration	Percentile					Mean	s.d.
	0	25	50	75	100										Quality	0	25	50	75	100		
Al	0	165	193	218	343	186.2	48	ICP-MS	%	5	20	0.75	0.70	19%	Good	1.52	4.86	5.29	5.63	7.48	5.12	0.81
Si	10	3242	3526	3727	6859	3379	612.4	HH-XRF	%	11	21	0.64	4.74	15%	Good	4.70	26.88	29.01	30.48	52.41	27.90	4.41
P	0	0	0	18	4335	27	149.5	ICP-MS	ppm	5	20	0.95	284	27%	Good	525	532	589	672	28,751	752	1049
S	0	542	713	900	15,437	739.3	334.6	ICP-MS	%	1	21	0.87	0.37	47%	Good	−0.42	0.92	1.34	1.80	37.58	1.40	0.82
Cl	0	62	86	118	10,245	127.5	259.1															
K	75	9971	11,078	11,969	19,499	10,708	2166.7	ICP-MS	%	1	20	0.87	0.29	27%	Good	−0.14	2.13	2.38	2.58	4.31	2.30	0.50
Ca	171	41,181	56,020	71,774	543,880	70,180	55,055.9	ICP-MS	%	5	20	0.96	0.96	24%	Good	1.44	4.08	5.10	6.18	33.91	6.05	3.69
Ti	0	6016	6702	7173	16,915	6291	1457.8	ICP-MS	%	1	20	0.82	0.04	23%	Good	0.05	0.29	0.32	0.33	0.72	0.30	0.06
V	0	228	319	726	12,408	713	998.1	ICP-MS	ppm	11	23	0.94	90	43%	Good	−14	75	101	262	4356	256	377
Cr	0	257	330	422	8957	342.7	182.2	ICP-MS	ppm	1	23	0.90	99	48%	Good	17	61	73	89	1546	75	31
Mn	27	1634	1937	3081	39,719	2916	2661.6	ICP-MS	ppm	1	19	0.97	48	31%	Good	−20	255	307	503	6780	475	456
Fe	1821	145,700	173,601	201,134	774,408	170,565	43,572.7	ICP-MS	%	1	23	0.31	1.11	35%	Fair	0.74	2.73	3.12	3.50	11.44	3.08	0.60
Ni	0	954	1131	1299	4221	1113	336.1	ICP-MS	ppm	11	22	0.61	14	82%	Fair	−24	31	39	46	127	38	16
Cu	0	802	913	1021	3994	900.8	206.5	ICP-MS	ppm	11	22	0.66	9	224%	Fair	−17	23	28	34	73	28	11
Zn	0	442	764	1386	245,738	1760	4591.1	ICP-MS	ppm	1	20	0.95	34	44%	Good	2	35	59	105	18,342	133	342
Ga	0	667	784	878	1488	746.9	208.3	ICP-MS	ppm	1	23	0.37	4	32%	Fair	3	11	12	13	20	12	2
As	0	0	31	142	1754	83.8	111.3	ICP-MS	ppm	5	22	0.65	4	47%	Good	5	7	10	14	58	11	6
Rb	0	2480	2880	3208	6033	2745	740.5	ICP-MS	ppm	1	20	0.73	15	25%	Good	16	80	90	99	172	87	19
Sr	544	3933	4238	4574	25,174	4426	1029.3	ICP-MS	ppm	11	20	0.89	23	15%	Good	69	124	135	148	460	142	38
Y	0	465	578	696	21,770	613.7	383	ICP-MS	ppm	1	22	0.08	10	44%	Poor	17	20	21	22	202	22	3
Zr	0	2607	3156	3773	7980	3147	957.3	ICP-MS	ppm	1	23	0.10	21	36%	Fair	43	58	61	65	90	61	6
Ba	0	302	400	538	54,199	466.6	496	ICP-MS	ppm	11	23	0.87	336	39%	Good	−38	378	485	631	10,072	549	355
Ce	0	57	84	111	1075	83.9	42.6	ICP-MS	ppm	5	23	0.04	20	43%	Poor	0	42	45	47	58	45	4
Sm	0	141	172	201	627	167.7	52.9															
Yb	0	0	0	157	3167	107.5	188.2															
Ta	69	1008	1108	1208	1913	1100	160.9	ICP-MS	ppm	1	23	0.08	0	38%	Poor	0	1	1	1	1	1	0
Pb	0	146	224	301	689	224.4	113	ICP-MS	ppm	11	22	0.35	4	38%	Fair	2	11	13	14	22	12	3
Po	0	141	201	261	715	202.9	90.2															
Th	0	155	232	307	672	230.6	111.2	ICP-MS	ppm	11	23	0.28	3	41%	Fair	1	7	8	9	13	8	2
U	0	105	181	257	2527	184.6	113.9	ICP-MS	ppm	1	22	0.32	3	57%	Fair	2	4	5	6	40	5	2

Table 2
Summary statistics for all 26 calibrated elements and element ratios, broken down by Formation and, within the Montney Formation, by substage. Negative values where present are outputs of correction equations used to convert ITRAX counts per second measurements to quantitative values.

		Al	Si	P	S	K	Ca	Ti	V	Cr	Mn	Fe	Ni	Cu	Zn	Ga	As	Rb	Sr	Y	Zr	Ba	Ce	Ta	Pb	Th	U	Cr/Al	Ti/Al	Rb/(Rb + K)	Al/(Al + K)
		%	%	ppm	%	%	%	%	ppm	ppm	ppm	%	ppm	ppm	ppm	ppm	ppm	ppm	ppm	ppm	ppm	ppm	ppm	ppm	ppm	ppm	ppm	x 10^4		Rb x 10^4	
Doig	mean	3.90	19.70	3859	1.74	2.13	13.24	0.19	778	79	165	1.91	55	29	399	8	20	57	284	26	56	246	51	0	11	4	4	19.81	0.05	0.96	0.66
Formation	s.d.	0.75	3.68	3786	0.81	0.71	3.82	0.05	738	32	62	0.41	29	16	1031	2	14	16	58	8	4	154	4	0	3	1	2	6.18	0.01	0.01	0.05
	median	4.15	19.84	2834	1.83	2.37	11.88	0.20	464	84	147	1.95	56	30	101	8	17	60	282	24	56	218	50	0	11	4	4	19.73	0.05	0.96	0.64
	min	2.16	11.37	525	−0.42	0.26	8.03	0.06	−7	17	36	0.88	4	0	2	3	5	16	182	17	44	−38	36	0	3	1	2	4.38	0.02	0.95	0.56
	max	5.35	35.29	24,178	4.49	3.20	23.07	0.30	2700	169	518	3.36	127	60	18,342	13	58	92	460	96	72	897	58	1	19	8	11	40.44	0.07	0.99	0.94
Sunset	mean	3.80	30.35	1221	0.66	1.79	8.76	0.23	28	52	218	1.77	28	21	69	11	6	63	185	24	70	407	46	1	11	7	5	13.79	0.06	0.97	0.68
Prarie	s.d.	0.78	3.93	1732	0.53	0.51	2.03	0.06	25	12	70	0.41	9	5	275	2	4	15	19	9	6	152	6	0	2	1	2	2.64	0.01	0.00	0.03
Formation	median	3.73	30.65	525	0.56	1.78	8.35	0.24	22	51	204	1.70	27	21	32	11	5	62	183	21	71	385	47	1	11	7	5	13.52	0.06	0.97	0.68
	min	1.96	17.02	525	−0.30	0.61	5.73	0.09	−8	20	39	1.02	10	5	2	3	5	23	153	17	44	157	2	0	4	4	2	5.42	0.02	0.96	0.61
	max	5.66	39.30	14,570	5.58	2.98	26.73	0.36	187	101	556	4.28	81	35	5545	16	50	106	333	106	89	959	55	1	17	10	11	25.55	0.08	0.98	0.87
Montney	mean	5.21	28.00	629	1.42	2.32	5.76	0.31	249	75	495	3.16	38	28	127	12	11	89	137	22	61	556	45	1	13	8	5	14.28	0.06	0.97	0.69
Formation	s.d.	0.73	4.10	212	0.81	0.46	3.47	0.05	355	19	465	0.52	15	11	291	2	6	18	27	2	5	310	4	0	3	1	2	2.95	0.01	0.00	0.03
(all)	median	5.34	29.05	587	1.35	2.39	5.02	0.32	102	74	315	3.17	39	28	60	12	10	91	134	21	61	494	45	1	13	8	5	14.06	0.06	0.97	0.69
	min	1.61	4.70	525	−0.42	−0.14	2.24	0.05	−14	17	−18	0.74	−24	−17	2	3	5	16	73	17	43	113	5	0	2	1	2	3.19	0.01	0.96	0.59
	max	7.48	36.79	7096	37.58	4.31	33.91	0.72	4356	169	6780	11.44	119	73	12,153	20	48	172	443	202	90	7359	58	1	22	13	34	29.47	0.13	1.00	1.04
Montney	mean	5.11	28.64	624	1.09	2.34	6.19	0.31	431	63	350	2.85	41	27	199	12	12	84	141	22	65	464	45	1	13	8	5	12.43	0.06	0.97	0.69
Formation	s.d.	0.64	3.83	291	0.59	0.40	2.60	0.05	466	13	198	0.37	17	10	401	2	6	14	17	3	5	253	4	0	3	1	2	2.00	0.01	0.00	0.02
(Spathian)	median	5.22	29.62	568	1.01	2.42	5.42	0.32	268	64	290	2.82	41	27	82	12	11	87	137	22	65	426	44	1	13	8	5	12.25	0.06	0.97	0.69
	min	1.61	7.21	525	−0.42	0.26	3.92	0.07	−10	17	139	1.30	−17	−13	2	4	5	18	98	17	43	113	5	0	2	2	2	3.91	0.03	0.96	0.59
	max	6.57	35.71	7096	9.61	3.33	27.10	0.55	4356	137	1966	6.39	119	73	12,153	19	48	117	328	202	78	7359	58	1	20	12	34	28.18	0.10	0.99	0.89
Montney	mean	5.16	26.56	624	1.60	2.19	6.39	0.29	113	77	764	3.31	34	24	71	11	12	90	145	21	58	596	45	1	12	8	5	14.79	0.06	0.98	0.71
Formation	s.d.	0.85	4.88	97	0.85	0.49	4.68	0.06	86	18	671	0.52	15	10	108	3	6	21	32	1	5	360	5	0	2	2	2	2.84	0.01	0.00	0.03
(Smithian)	median	5.36	27.85	602	1.54	2.30	4.72	0.31	87	80	544	3.35	37	27	59	12	10	95	139	21	59	517	45	1	12	8	5	15.06	0.06	0.98	0.70
	min	1.79	4.70	525	−0.42	0.04	2.60	0.06	−14	17	189	0.83	−24	−17	2	3	5	16	95	17	43	154	28	0	2	1	2	4.03	0.02	0.96	0.60
	max	7.13	33.52	1208	24.52	3.59	33.91	0.41	601	130	6780	8.73	66	62	6662	20	39	152	443	56	74	5104	58	1	22	11	12	29.47	0.09	1.00	0.98
Montney	mean	5.39	28.98	646	1.64	2.35	4.08	0.31	83	92	399	3.51	35	35	69	13	8	95	119	21	60	703	45	1	12	9	5	17.16	0.06	0.98	0.70
Formation	s.d.	0.60	2.49	144	0.77	0.40	1.96	0.04	25	12	240	0.36	11	10	166	1	3	16	21	2	4	286	4	0	2	1	2	1.72	0.00	0.00	0.02
(Dienerian)	median	5.49	29.41	630	1.65	2.41	3.43	0.32	81	93	309	3.53	38	35	52	13	8	98	114	21	60	633	45	1	12	9	5	17.12	0.06	0.98	0.70
	min	2.18	15.61	525	−0.41	−0.14	2.24	0.05	8	17	−18	0.74	−18	−4	2	3	5	18	73	17	43	273	29	0	3	3	2	3.19	0.01	0.96	0.61
	max	7.48	36.79	4301	37.58	4.31	26.18	0.72	277	147	2007	11.44	58	62	10,942	17	23	172	312	155	90	3216	58	1	19	13	11	29.27	0.13	1.00	1.04
Montney	mean	5.93	28.43	636	2.53	3.19	3.29	0.34	120	104	292	3.76	39	36	49	13	12	108	98	22	59	575	43	1	13	9	5	17.65	0.06	0.97	0.65
Formation	s.d.	0.47	1.64	85	1.12	0.32	0.92	0.03	26	11	164	0.39	7	6	90	1	4	13	7	1	3	174	3	0	2	1	2	1.80	0.00	0.00	0.02
(Griesbachian)	median	5.97	28.66	626	2.42	3.25	2.88	0.35	119	105	220	3.70	41	36	34	13	11	111	98	22	59	538	43	1	13	9	5	17.54	0.06	0.97	0.65
	min	4.04	23.30	525	1.06	1.53	2.30	0.22	51	67	103	3.12	14	19	3	8	5	49	74	18	51	301	34	0	8	6	2	11.66	0.04	0.97	0.60
	max	7.22	31.77	972	25.52	4.02	6.82	0.45	246	169	876	10.31	53	50	1895	17	27	149	121	32	65	1497	54	1	18	12	12	29.14	0.07	0.98	0.76
Belloy	mean	3.30	37.29	3067	1.59	1.32	4.01	0.18	116	290	115	2.57	38	33	167	13	8	70	134	21	53	1545	42	1	10	8	8	110.32	0.05	0.98	0.75
Formation	s.d.	0.65	3.93	291	0.59	0.40	2.71	0.05	466	13	202	0.38	17	10	400	2	6	14	17	3	5	253	4	0	3	1	2	2.01	0.01	0.00	0.02
	median	2.74	39.48	860	1.29	0.90	2.73	0.14	113	242	103	2.44	42	35	40	13	6	66	109	19	52	825	44	1	10	9	7	96.69	0.05	0.99	0.75
	min	1.52	25.21	525	−0.11	−0.06	1.44	0.05	33	34	−20	1.03	−9	7	2	8	5	20	69	17	43	386	0	0	3	4	2	15.12	0.03	0.97	0.56
	max	6.41	52.41	28,751	9.07	3.54	14.85	0.45	244	1546	279	5.42	67	47	8718	17	30	129	400	52	79	10,072	52	1	17	12	40	660.49	0.13	1.00	1.04

dolostone or other bioclasts. Ca decreases across the Permian-Triassic boundary, from an average of 4.01% (s.d. = 2.71%) in the Belloy Formation to an average value of 3.21% (s.d. = 0.92%) in the Griesbachian interval of the Montney Formation (which is devoid of observable carbonate). While this remains a typical value for Montney siltstone (Fig. 4), the presence of carbonate beds from the Dienerian onward elevates the average value for the full formation to 5.76% (s.d. = 3.47%), with the highest values (approximately 25%) are seen in the Smithian, coincident with deposition of bioclastic tempestites. The Sunset Prairie Formation (mean = 8.76%, s.d. = 2.03%) and Doig Formation (mean = 13.24%, s.d. = 3.82%) both show elevated Ca relative to the Montney Formation.

Aluminum increases across the Belloy-Montney contact, from an average of 3.30% (s.d. = 0.65%) to an average of 5.21% (s.d. = 0.73%). However, considerable variability is seen in throughout the Montney Formation, with the highest values seen in the Greisbachian aftermath of the end-Permian mass extinction (mean = 5.93%, s.d. = 0.47%). Two pronounced Al minima are seen in the Montney Formation, one associated with the calcareous Pocketknife Member, and another in the lower Spathian, coincident with excursions in provenance proxies (Fig. 4; see below). Al is low in the sandy Sunset Prairie Formation (3.80%, s.d. =0.78%), but increases somewhat in the Doig Formation (mean = 3.90%, s.d. = 0.75%).

4.2. Provenance and weathering

One method of assessing provenance is to look at changes in the differentiation of the parent material, a signal that can be preserved as geochemical signatures even in mature marine sediments (McLennan et al., 1993). While high iron and magnesium content are defining characteristic of mafic source rocks, Mg was not measured by the ITRAX scanner, and Fe yielded only a 'fair' calibration (Table 1) – it can also be precipitated authigenically from seawater (Lyons and Severmann, 2006), limiting its utility as a provenance proxy. In constructing ratios to determine differentiation, we relied on Cr and Ti, both of which are enriched in mafic and intermediate source rocks relative to felsic rocks (McLennan et al., 1993), and both of which showed strong correlations between ICP-MS measurements and the ITRAX XRF dataset (Table 1). Additionally, Ti is essentially immobile in the marine environment, and the Ti/Al ratio of marine sediments likely represents that of the sediment source (Thomson et al., 2006). Ti/Al and Cr/Al ratios (Fig. 4) were both used to assess the contribution of relatively undifferentiated sediment, which is likely to be derived from the andesitic, volcanically active Yukon-Tanana arc, as opposed to the mature, low-gradient margin of North America.

The Ti/Al ratio increases slightly across the Belloy-Montney formation contact, from an average value of 0.05 in the Belloy Formation (s.d. = 0.01) to 0.06 in the Montney Formation (s.d. = 0.01). While little variation is seen between substages of the Montney, a slight decrease can be observed in the later Smithian, and an increasing trend in the lower Spathian can be identified (Fig. 4). Likewise, an increase can be discerned from the Sunset Prairie Formation into the overlying Doig Formation. The Cr/Al proxy shows similar but distinct stratigraphic patterns, with one of the most notable differences being a sharp decrease across the Permian-Triassic boundary, from an average value of 110.32 in the Belloy Formation (s.d. = 2.01) to an average of 14.28 in the Montney Formation (s.d. = 2.95). While there is little stratigraphic variation in the Montney, a pattern similar to the Ti/Al proxy can be discerned, with declining values in the Smithian, and a positive excursion in the lower Spathian, beginning at approximately 2350 mbs, coincident with end of the lower Spathian increasing trend in Ti/Al (Fig. 4). Values in the Sunset Prairie Formation are similar to the Montney, but elevated values are seen in the Doig Formation (mean = 19.81, s.d. = 6.18).

Ratios of elements that show different responses to weathering or erosional processes are widely used to trace the provenance and transport history of sediments (Nesbitt and Young, 1982). The intensity of chemical weathering can be assessed by determining ratios of cations predominantly hosted in the clay and feldspar fraction, such as Al, Rb, and K. Since Al is less soluble than K, and Rb is more likely to be retained during intense chemical weathering (Helmke and Sparks, 1996), high Al/(Al + K) and Rb/(Rb + K) ratios are indicative of mature sediments that experienced chemical alteration during transport, whereas low ratios indicate immature material that has been subjected to minimal chemical weathering. Clay minerals are generally rare in the Montney Formation, with even clay-sized sediment dominated by quartz, alkali feldspars, and muscovite, which is often reported as illite at small grain sizes (Moslow et al., 2018). The proxies reported here likely reflect the weathering of feldspars (Al:K ratio 1:1 in orthoclase) and production of illite and/or muscovite (nominal Al:K ratio > 3:1).

Weathering proxies exhibit similar patterns throughout the core (Fig. 4), starting with a significant decrease across the Permian-Triassic boundary. Al/(Al + K) decreases from an average value of 0.75 in the Belloy Formation to 0.65 in the Griesbachian substage of the Montney Formation, while Rb/(Rb + K) exhibits a similar decrease from 0.98 to 0.97. Both proxies then increase gradually through the Dienerian and lower Smithian, reaching a local maximum in the middle Smithian. Both proxies show relatively consistent values throughout the Spathian substage of the Montney Formation, although some cyclical behavior is evident, corresponding to sedimentologically recognized (Moslow et al., 2018) and astronomically tuned (Shen, 2018) parasequences (Fig. 4). Both increase slightly in the Sunset Prairie Formation before decreasing again in the Doig Formation.

4.3. Redox and productivity

A variety of transition metals can accumulate in sediment under reducing water column conditions, and can thus serve as useful proxies for anoxia in the depositional environment (Tribovillard et al., 2006; Algeo and Liu, 2020). Of these, vanadium and zinc showed the strongest correlations between ITRAX and ICP-MS measurements in c-65-F (Table 1), and will thus be the main trace metal proxies considered in this study (Fig. 5). Other potential redox sensitive metals, such as Ni, Cu, and U showed much weaker correlations with ICP-MS data.

Vanadium is generally quite low in the Belloy Formation (mean = 116 ppm, s.d. = 466 ppm) and through the Griesbachian (mean = 120 ppm, s.d. = 26 ppm), Dienerian (mean = 83 ppm, s.d. = 25 ppm), and Smithian (mean = 113 ppm, s.d. = 86 ppm) intervals of the Montney Formation. Significant excursions, to values above 1000 ppm and as high as 4000 ppm, are seen periodically beginning in the lower Spathian, alternating with lower values (Spathian mean = 430 ppm, s.d. = 466 ppm; Fig. 5). The Sunset Prairie Formation shows low values of V (mean = 28 ppm, s.d. = 25 ppm), while values are quite elevated in the Doig Formation (mean = 778 ppm, s.d. = 738 ppm). Unlike vanadium, Zn shows a substantial decrease across the Permian-Triassic boundary, from an average of 167 ppm in the Belloy Formation (s.d. = 400 ppm) to an average of 49 ppm in the Griesbachian interval of the Montney (s.d. = 90 ppm). Similarly low values are seen in the Dienerian (mean = 69 ppm, s.d. = 165 ppm) and Smithian (mean = 71 ppm, s.d. = 108 ppm) substages of the Montney. Like vanadium, a series of elevated intervals, with values as high as 12,000 ppm, is seen in the lower Spathian (substage mean = 199 ppm, s.d. = 400 ppm). Values in the Sunset Prairie Formation average 69 ppm (s.d. = 275 ppm), rising to an average of 399 ppm in the Doig Formation (s.d. = 1031 ppm).

Manganese can accumulate in sediment via operation of the 'manganese shuttle', with dissolution of manganese oxyhydroxides in reducing settings and its precipitation as insoluble phases in oxic sediment pore water (Tribovillard et al., 2006; Calvert and Pedersen, 2007). Mn shows some correlation with Ca in c-65-F ($r^2 = 0.29$) and is elevated in the same thin calcisphere dolostone beds where Ca is most abundant, suggesting that Mn accumulation may be associated with carbonate deposition or dolomitization in this system. However, there is a distinct

peak in Mn content, to values as high as 0.6%, in the upper Smithian Altares Member (Fig. 5).

Sulfur can be a useful proxy for euxinic conditions, since it will tend to accumulate (mostly as pyrite) in environments where sulfate is being reduced by bacteria. While the geochemistry of arsenic is complex, this element is generally retained in the sediment as a cation in sulfide minerals (Tribovillard, 2020). Both of these elements showed a good correlation between ITRAX data and ICP-MS results (Table 1). Sulfur content shows little change across the contact between the Belloy Formation (mean = 1.59%, s.d. = 0.59%) and the overlying Montney (full formation mean = 1.42%, s.d. = 0.81%), but considerable variability between Montney substages. Sulfur is elevated in the Griesbachian (mean = 2.53%, s.d. = 1.12%), but decreases in the Dienerian (mean = 1.63%, s.d. = 0.76%) and Smithian (mean = 1.61%, s.d. = 0.85%). Values in the Spathian show some variability, but are generally lower than those in the Smithian (mean = 1.09%, s.d. = 0.59%). Sulfur in the Sunset Prairie Formation is quite low (mean = 0.81%, s.d. = 0.53%), though the Doig Formation has values comparable to those seen in the Montney (mean = 1.74%, s.d. = 0.81%). Like sulfur, arsenic shows significant variability within the Montney Formation. Values are elevated in the Griesbachian (mean = 12 ppm, s.d. = 4 ppm), decline through the Dienerian (mean = 8 ppm, s.d. = 3 ppm), then increase again in the Smithian (mean = 12 ppm, s.d. = 6 ppm; Fig. 5). The Spathian contains several discrete intervals with As content of nearly 50 ppm, though average values are comparable to the underlying Smithian (mean = 12 ppm, s.d. = 6 ppm). Arsenic is low in the Sunset Prairie Formation (mean = 6 ppm, s.d. = 4 ppm), but elevated in the Doig Formation (mean = 20 ppm, s.d. = 14 ppm).

Developing geochemical proxies for primary productivity is difficult, not least because it is convolved with redox conditions. Phosphorus is a major component of organic matter, and while it is more likely to be retained under oxic conditions (Schoepfer et al., 2015), it is often abundant enough in sediments to be useful over a range of conditions. Furthermore, it is among the only elements useful for distinguishing between upwelling zones and other anoxic environments (Brumsack, 2006). Across the Permian-Triassic boundary, P content decreases from an average of over 3000 ppm (s.d. = 291 ppm) in the Belloy Formation to an average of just over 600 ppm (s.d. = 212 ppm) through the rest of the Montney Fm (Fig. 5). This value is relatively consistent across Early Triassic substages, although several elevated intervals with values as high as 7000 ppm are seen in the lowest Spathian. Phosphorus is elevated in Anisian strata relative to the Montney, with a mean value of approximately 1200 ppm (s.d. = 1732 ppm) in the Sunset Prairie Formation and approximately 3900 ppm in the Doig Formation (s.d. = 3786 ppm).

4.4. Principal components

Principal Components Analysis yielded a total of 23 PCs from the compiled dataset. While the first five components have eigenvalues >1 (Table S3), the percentage of variance explained drops off steadily after the first two PCs (Fig. S3). The first four PCs cumulatively explain ~66% of total variance in the dataset, and it is these four that will be considered further in this study (Fig. 3).

The loadings associated with each of the first four principal components can be seen in Fig. 3. Based on these loadings interpretations of the principal environmental controls on each PC are discussed below. The PC scores of individual horizons are plotted stratigraphically in Fig. 6, and discussed further in Section 5.

Principal Component 1- Principal Component 1 explains 38.08% of variance in the total data set (Fig. S3). Of the 'elements with a 'Good' calibration rating, it shows strong ($r > 0.75$) positive correlations with Al, Si, K, Ti, and Rb, all of which are most likely to be found in the terrigenous clastic fraction, in the form of quartz silt (Si), rutile/ilmenite/titanite (Ti) and feldspars or clays (Al, K, Rb). PC1 shows a very strong ($r < -0.90$) negative correlation with Ca, and lesser negative correlations with ($r < -0.50$) with Mn and S (Fig. 3), suggesting that PC1 predominantly reflects the relative clastic vs. carbonate composition of the sediments. A number of trace elements with 'Fair' calibration ratings also have positive correlations ($r > 0.50$) with PC1, including Ni, Cu, Ga, Pb and Th. In some systems Ni and Cu can track marine redox and productivity conditions (Tribovillard et al., 2006), however their correlation with PC1 here suggests that Cu and Ni are primarily carried in terrigenous material and do not strongly reflect the water chemistry of

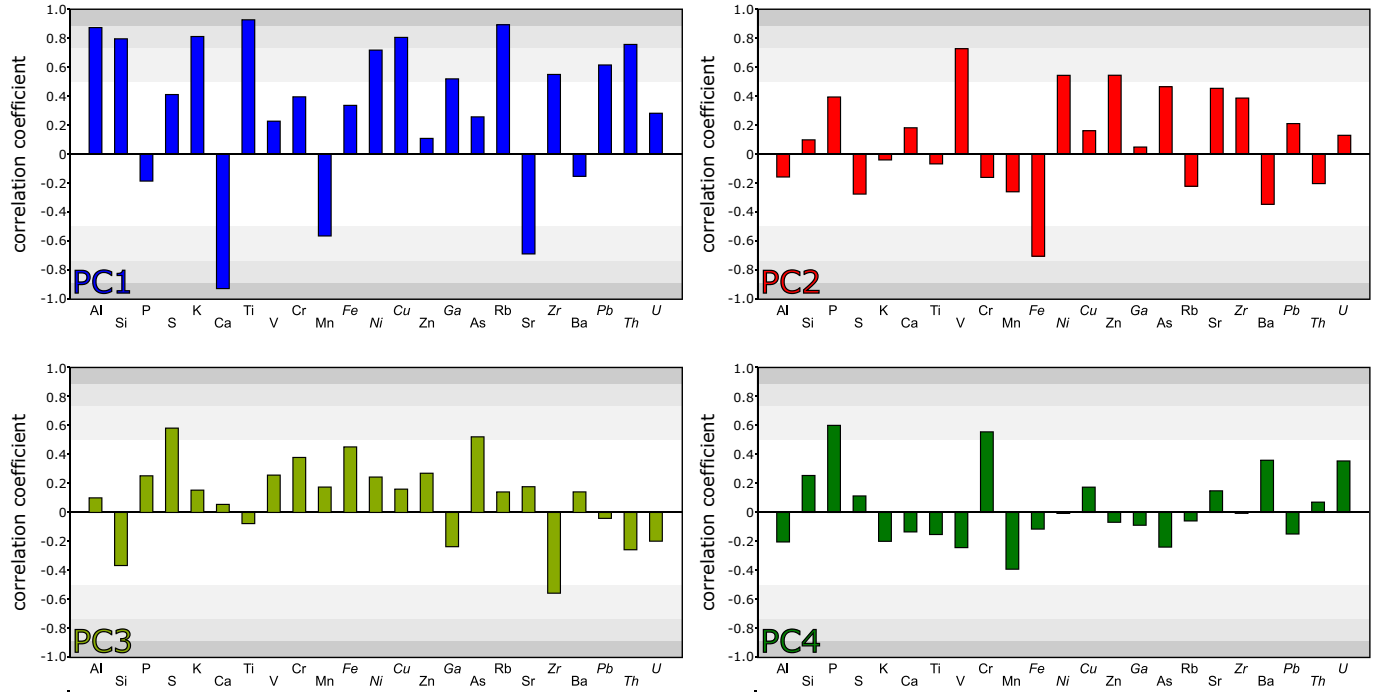

Fig. 3. Loadings plots showing the correlation coefficients between the first four principal components with each of the elements in the dataset. Colors correspond to those used in Figs. 7 and S3. Gray fields indicate correlation coefficients with absolute values >50%, 75%, and 90%.

the depositional basin.

Principal Component 2 – Principal Component 2 is responsible for 12.56% of variance in the complete dataset (Fig. S3). Its strongest positive correlation ($r > 0.60$) is with vanadium, and its strongest negative correlation is ($r < -0.60$) with iron (which only has a 'Fair' calibration). Weaker positive correlations can be observed with P, Ni, Zn, As, and Sr (Fig. 3). Vanadium is concentrated in sediments under anoxic conditions, suggesting that PC2 may be primarily capturing fluctuations in redox conditions. However, unlike many redox-sensitive metals, vanadium is not retained in solid solution with sulfides (Tribovillard et al., 2006), and somewhat surprisingly, PC2 shows a weak negative correlation with sulfur. Combined with the negative correlation with iron, this may indicate that PC2 primarily reflects suboxic or ferruginous conditions, as distinct from euxinic conditions characterized by free sulfide (see PC3 below). Correlated as it is to redox sensitive trace elements, this component may only capture anoxia effectively when inventories of dissolved trace elements were available in the water column.

Principal Component 3 – Principal Component 3 is responsible for 8.69% of variance in the dataset (Fig. S3). Its strongest positive correlations ($r > 0.50$) are with sulfur and arsenic, though it shows weaker positive correlations with iron and chromium, and weak ($r < 0.30$), but positive correlations with a number of sulfide forming cations (Ni, Cu, Zn). It also shows a strong negative correlation ($r < -0.50$) with Zr, and a weaker negative correlation with Si (Fig. 3). As arsenic is mainly hosted in sediment as a substituted cation in sulfide minerals, or bonded to sulfurized organic complexes (Tribovillard, 2020), and other sulfide-forming cations are positively correlated with PC3, it is likely this component is at least partially capturing the sulfide content of sediments, which can be related to euxinia (free hydrogen sulfide) in the water column or sediment pore water. This interpretation is supported by the presence of dispersed pyrite framboids throughout Griesbachian strata, and pyrite crystals and pyritized bioclasts in the Smithian interval, both of which correspond to elevated values of PC3.

The negative correlation with Zr and Si suggests that PC3, and thus euxinia, is inversely correlated with the coarser-grained silt/sand fraction of the sediment, where Zr is likely to be hosted. This may be a capturing a real phenomenon, reflecting that euxinia is more likely to develop in deeper water facies, where the finest sediments are deposited. Coarser, more porous sediment may also inhibit the development of sulfide by allowing oxygen to circulate into sedimentary pore water.

Principal Component 4 – Principal Component 4 explains 6.54% of variance in the dataset (Fig. S3), and shows strong ($r > 0.50$) positive correlations only with P and Cr. The strongest negative correlations are with Mn, V, and As, all redox sensitive elements (Fig. 3). Since P enrichment often reflects high productivity as a result of upwelling (Brumsack, 2006) and Cr can be transported to the sediment via organic matter, but is not typically retained in sulfides (Tribovillard et al., 2006), we interpret PC4 as representing the incursion of nutrient-rich waters, separated via PCA from its potential redox implications, which are captured by the more significant principal components.

5. Interpretation of geologic history

5.1. The uppermost Permian and lower Induan: Griesbachian substage

The end-Permian mass extinction in core c-65-F is characterized by dramatic geochemical changes. Some of the apparent complexity may be due to the position of western Pangaea in an active coastal upwelling zone during the latest Permian. The extinction horizon coincides with a rapid drop in phosphorus content (also reflected in PC4; Fig. 6). This may reflect decreased P retention under euxinic conditions, but may also be a result of the termination of coastal upwelling and concomitant decrease in primary productivity that has been observed elsewhere along the western margin of Pangaea (Schoepfer et al., 2013; Grasby et al., 2020).

The Griesbachian interval is characterized by low Cr/Al and Ti/Al ratios (Fig. 4), suggesting that the principal sediment source had a differentiated composition – most likely this was felsic rocks and reworked sediments from the North American continent. Al and Si content both increase (Fig. 4), indicating a transition to the regime of terrigenous sediment influx to marine environments that is characteristic of the Early Triassic on a global scale (Algeo and Twitchett, 2010; Algeo et al., 2011). The low values of the Al/(Al + K) and Rb/(Rb + K) weathering proxies relative to later Montney strata (Fig. 4) indicate that Griesbachian sediment experienced comparatively little chemical weathering during its transport from source to basin. This may reflect devastation of terrestrial plant communities and destabilization of soils, followed by accelerated physical erosion of exposed bedrock with minimal chemical weathering (Algeo and Twitchett, 2010; Hermann et al., 2011; Knies et al., 2022). Aeolian sediment transport, from the arid margin of North America (Davies et al., 1997; Zonneveld and Moslow, 2018), would also have reduced the sediments' exposure to aqueous weathering reactions.

Griesbachian sediments show elevated levels of arsenic and sulfur relative to the uppermost Permian and overlying Dienerian, suggesting euxinic conditions in the environment. Euxinic conditions were widespread in the global ocean during the earliest Triassic (Grice et al., 2005; Hays et al., 2007; Meyer et al., 2008; Zhang et al., 2018a; Grasby et al., 2021), and may have been advected into the Montney depositional basin from the paleo-Pacific (Fig. 7B; Hays et al., 2007; Zhang et al., 2017). The uniformly low *P* values (Fig. 5), and low scores of PC4 (Fig. 6), throughout the Lower and Middle Montney rule out high productivity as a driver of reducing conditions. Despite this evidence for euxinia, some trace elements (i.e., V and Zn) decrease across the extinction boundary (Fig. 5). The absence of enrichments in redox sensitive transition metals despite enrichment in sulfur suggests these metals may have been depleted, either globally (Zhang et al., 2018a), or locally within the basin.

5.2. The upper Induan: Dienerian substage

The Dienerian substage has been interpreted as a temporary interval of relief from ecological stresses based on sections from South China and elsewhere (Shen et al., 2015; Wei et al., 2015), and data from core c-65-F generally support this interpretation. Chemical maturity appears to increase above Griesbachian levels (Fig. 4). This may ultimately result from the recovery of terrestrial plant ecosystems, as has been observed on the northern Gondwana region (Hermann et al., 2011), with soil stabilization leading to longer transport pathways for terrigenous sediment and less aeolian deposition (Fig. 7C). Increasing Cr/Al and Ti/Al ratios suggesting a greater proportion of sediment derived from the arc bounding the western margin of the basin in this interval (Fig. 4). While this may have been driven by increased volcanic activity or tectonic steepening of the western basin gradient, ash beds have not yet been recognized beds in the core, and the signal may just as easily reflect a *relative* increase, due to continental North America no longer rapidly shedding sediment into the depositional basin. The maximum of apparent arc influence in the Lower Montney occurs from ~2500–2530 mbs, in the uppermost Dienerian Pocketknife Member.

Geochemical evidence also supports a period of relief from euxinic conditions. Sulfur and arsenic values decrease below Griesbachian levels throughout the Dienerian, while redox sensitive trace metals such as V and Zn remain low. While values of PC2 are consistent, values of PC3 decrease, likely indicating that there was less sulfide in the bottom water or sedimentary pore water (Fig. 6). This may represent a transition to suboxic or ferruginous, rather than euxinic, bottom water conditions, which would have been more favorable colonization of the basin by certain hypoxia-tolerant organisms.

Perhaps the most striking contrast with the Griesbachian substage is the appearance of carbonate, in the form of regularly spaced calcisphere dolostone horizons, composed of calcispheres. The uppermost Dienerian

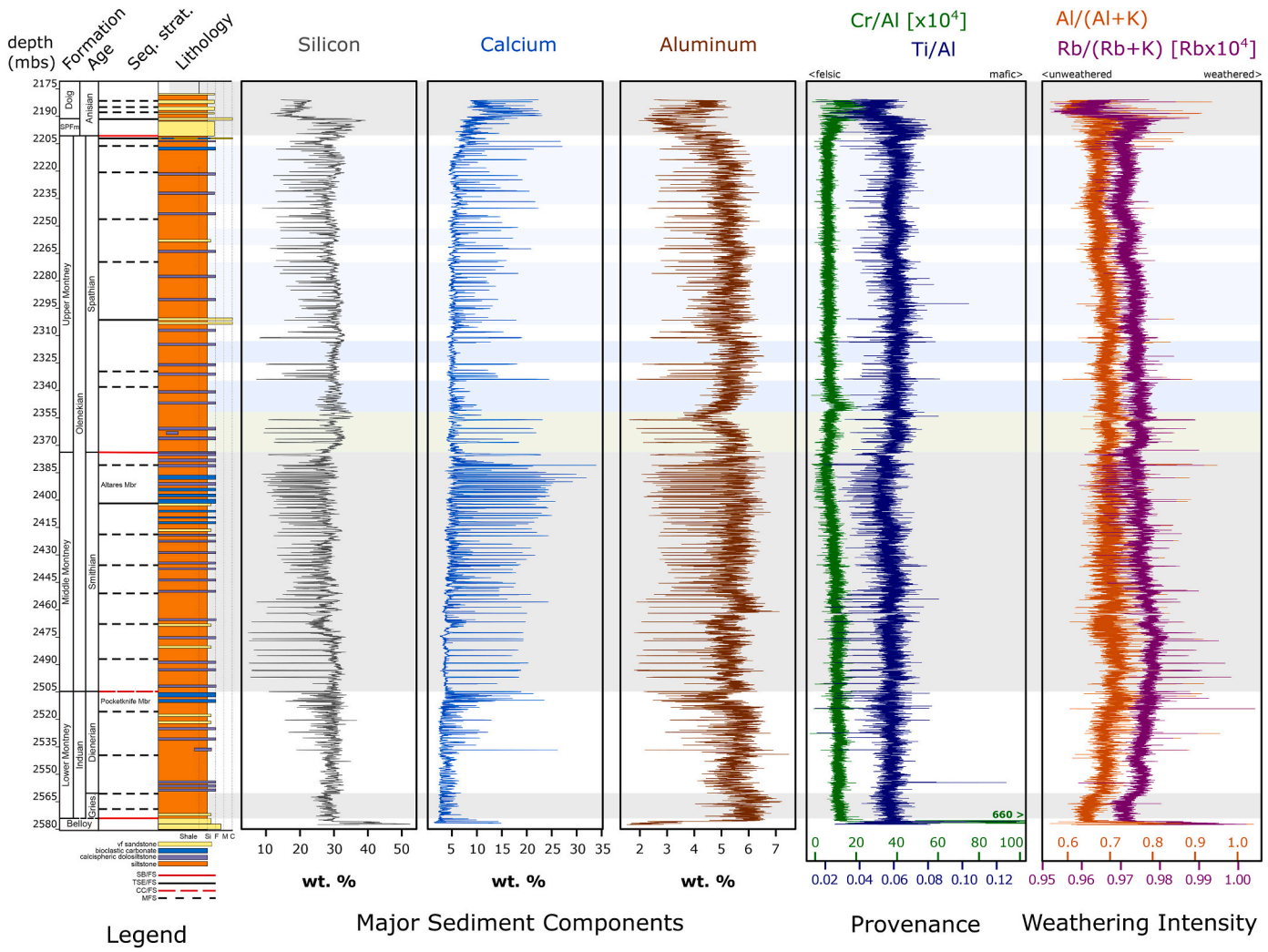

Fig. 4. Stratigraphic plot of elemental proxies for provenance and chemical maturity. SPFm. = Sunset Prairie Formation; SB/FS = Sequence Boundary/Flooding Surface; TSE/FS = Transgressive Surface of Erosion/Flooding Surface; CC/FS = Correlative Conformity/Flooding Surface; MFS = Marine Flooding Surface. Highlighted intervals in Spathian correspond to Fig. 8. Green: Panel D, Phosphatogenesis; Dark Blue: Panel F, early Spathian restriction; Light Blue: Panel G, Later Spathian restriction. (For interpretation of the references to color in this figure legend, the reader is referred to the web version of this article.)

also corresponds to the appearance of epifaunal *Claraia* biostromes (i.e., the Pocketknife Member; Moslow et al., 2018). *Claraia* first occurs in the lower Dienerian at c-65-F, but the presence of biostromes in the upper Dienerian may indicate more favorable conditions at the sediment-water interface. *Claraia* is widespread in Lower Triassic sediments globally, and is often regarded as a disaster taxon, able to opportunistically colonize suitable environments through planktic dispersal (Huang et al., 2018). The occurrence of *Claraia* biostromes in association with deep fault systems in the Montney Formation has led to the suggestion that these bivalves relied on chemotrophic symbionts for energy (Moslow et al., 2017). However, the appearance of *Claraia* coinciding with other evidence for more favorable conditions would seem to suggest they were opportunistically occupying an improving benthic habitat.

5.3. *The lower Olenekian: Smithian substage and sub-Spathian sequence boundary*

The lowest 25 m of the Smithian succession generally shows a continuation of Dienerian trends, with regularly-spaced calcispheric dolostone beds and no initial evidence for changes in provenance or water-column redox conditions. This incipient recovery was interrupted by the recurrence of euxinia in the lower Smithian, as recognized by elevated As and S content, and more positive PC3 scores, beginning at ~2470 mbs (Fig. 6). This reappearance of euxinia in the Smithian may reflect global changes in oceanographic conditions, in response to the well documented Smithian thermal maximum (Sun et al., 2012; Wei et al., 2015; Zhang et al., 2015, 2019a, 2019b; Song et al., 2019; Widmann et al., 2020). However, another unique feature of this interval is increasing manganese content (to values as high as 0.5 wt%; Fig. 5), which may reflect operation of the 'manganese shuttle' (Tribovillard et al., 2006) close to the sediment-water interface, with manganese being retained in sediment due to rapid deposition (see below). This implies a fluctuating redoxocline close to the sea floor, suggesting that euxinia may have developed primarily in sedimentary pore water rather than the water column.

However, the Smithian crisis at c-65-F differs from that identified elsewhere in that it does not coincide with a decline in carbonate production or deposition. Widmann et al. (2020) identified a 'carbonate crisis' during Phases 2 and 3 of the Smithian-Spathian transition, centered around an age of 249.5 Ma, while Zhao et al. (2020) identified a recovery of carbonate production in South China across the Smithian-Spathian boundary. While in many ways the Smithian interval of c-65-F appears to represent a return to a Griesbachian-like environment, bottom water conditions remained conducive to carbonate preservation, and regularly-spaced calcisphere dolostones continued to be deposited throughout this interval (Shen, 2018). The carbonate tempestites of the

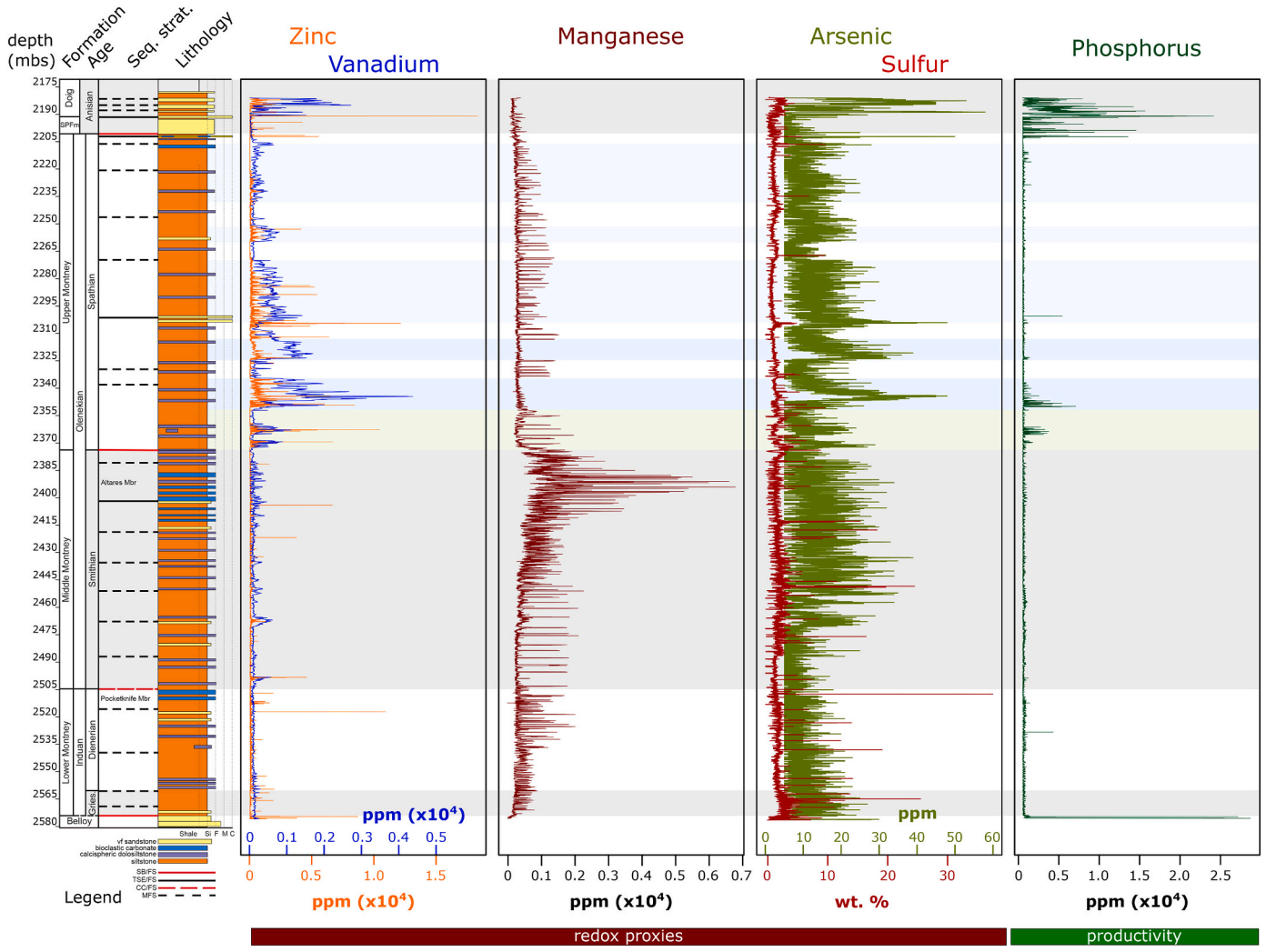

Fig. 5. Stratigraphic plot of elemental proxies for redox conditions and productivity. See Fig. 4 caption for explanation of stratigraphic column and highlighted intervals in Spathian.

Altares Member (Fig. 7D) were deposited in an interval centered around 249.5 Ma (i.e., the (*Scythogondolella mosheri – Sc. phryna* conodont biozones; Henderson et al., 2018), coincident with the 'carbonate crisis' of Widmann et al. (2020). This suggests continued production of carbonate sediment in shallow environments, with *Claraia* from more proximal settings having been reworked and transported basinward during this period of rapid deposition.

This second period of environmental disruption may also have affected terrestrial environments. The Smithian shows a reversal of the trend toward more arc-derived sediment, supporting the interpretation that turbidites in this interval are derived from the North American margin to the east (Davies et al., 2018; Moslow and Davies, 1997), rather than the arc to the west. The terrigenous component becomes increasingly chemically immature, though not to the same degree seen in the Griesbachian (Fig. 4). These observations are consistent with the global evidence for a 'spore spike' (Hermann et al., 2011) and increased aridity during the Smithian crisis (Lindström et al., 2020). In the Montney depositional setting, the loss of terrestrial vegetation led to rapid progradation of North American-derived sediment in this interval, resulting in facies offlap in the basin that eventually culminates in the sub-Spathian sequence boundary.

5.4. *The upper Olenekian: lower Spathian substage*

The Smithian substage, which coincides with the Middle Montney sequence in the study area, concluded with a major sequence boundary, affecting even distal environments such as the c-65-F depositional setting. The boundary can be recognized sedimentologically, as a truncated surface showing a transition from dolosiltstones to bituminous and phosphatic siltstones, though biostratigraphy indicates that deposition across this coplanar sequence boundary/flooding surface (Moslow et al., 2018) was continuous. The sedimentological change reflects paleoceanographic conditions that were significantly different from those recorded in the Lower and Middle Montney (i.e., the Griesbachian through Smithian substages).

The lowermost 15 m of the Spathian succession show some of the only detectable phosphorus enrichments of the Montney Formation (Fig. 5), as well as positive excursions in PC4, likely reflecting an interval of high productivity (Fig. 6). These phosphorus excursions coincide with elevated PC2 and PC3 scores, and minor enrichments in all redox sensitive elements, including sulfur and arsenic, indicating euxinia. This lowermost Spathian interval may record the resumption of coastal upwelling, likely in response to cooling climate conditions (Fig. 8A) and amelioration of the stratified oceanic water column (Song et al., 2019; Zhang et al., 2015). This coincides with the onset of a major global radiation in the diversity of nektic organisms, including ammonoids and

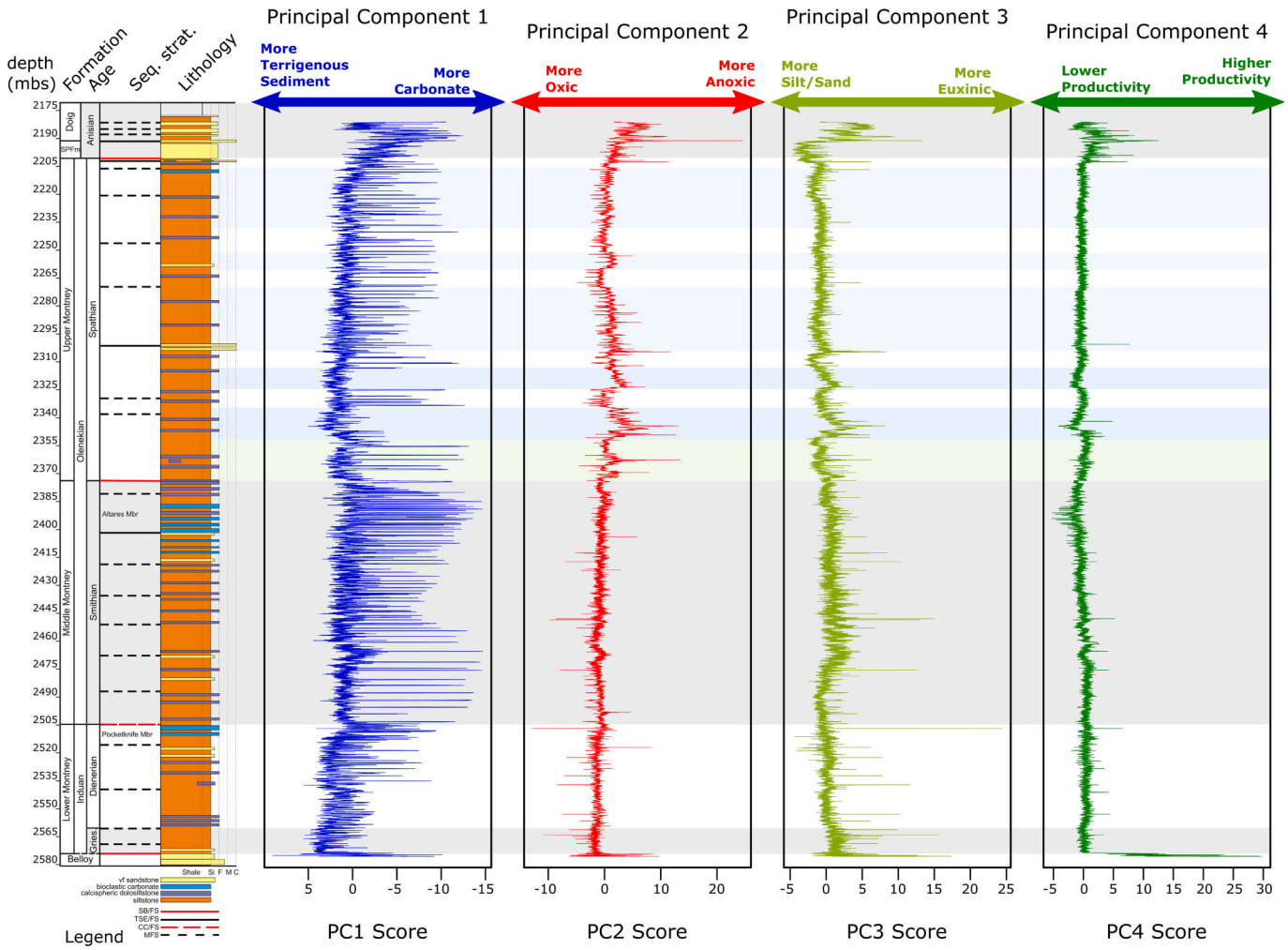

Fig. 6. Stratigraphic plot of principal component scores for the first four principal components derived from PCA. See Fig. 4 caption for explanation of stratigraphic column and highlighted intervals in Spathian.

conodonts (Zhang et al., 2019a, 2019b). As nutrient-rich waters flowed into the shallow Montney depositional basin, they would have fueled high primary productivity, with the decomposition of sinking organic matter driving the basin from ferruginous toward euxinic conditions.

This interval of upwelling terminates between 2345 and 2350 mbs, which correlates to a substantial but transient increase in the Cr/Al ratio, and a more muted increase in the Ti/Al ratio, both of which likely reflect the contribution of an arc sediment component (Fig. 4). These changes appear to be indicating a 'rejuvenation' of the Yukon-Tanana arc bounding the basin to the west, either via volcanic activity, or by tectonic uplift and steepening of the western basin gradient. This may be related to the development of east-dipping subduction outboard of the Yukon-Tanana arc (Nelson et al., 2006; Beranek and Mortensen, 2011). Olenekian sediments from the Yukon Territory show an increased component of ferromagnesian material, likely derived from the Yukon-Tanana arc, which was overriding the western margin of the North American craton in this interval (Beranek et al., 2010). This reactivation of the arc appears to have made the Yukon-Tanana terrane a more formidable barrier to water circulation. The depositional basin was transitioning in this interval from a marginal epeiric platform to a narrow foreland type basin, with downward flexure of the crust due to loading (Nelson et al., 2006). Depositional parasequences are easily recognized both sedimentologically (Euzen et al., 2018) and geochemically (see below).

Evidence for periodic anoxia dominates geochemical signals through the remainder of the Montney Formation. Two of these intervals of restriction can be identified in the lower Spathian (from 2307 to 2324 mbs and from 2335 to 2352 mbs), characterized by major enrichments in V and Zn (as well as As, though not S; Fig. 5). Scores for PCs 3 and 4 are also elevated (Fig. 6), showing an association with one another not seen in the Lower or Middle Montney. The appearance of substantial V and Zn enrichments suggests that oceanic inventories of these trace elements may have begun to recover from end-Permian and Smithian depletion at this time.

While phosphorus enrichments continue into the lowermost of these intervals, they are not seen thereafter, suggesting that anoxia in the basin was not driven by western boundary upwelling during most of the Spathian. Instead, anoxia was likely driven by basinal restriction, at times when the Yukon-Tanana arc was served as an effective barrier to circulation. If coastal upwelling did indeed continue to occur, its effects were most likely felt outboard of the Yukon-Tanana arc (Fig. 8B). While it is unclear if productivity was unusually low within the depositional basin, bottom water conditions were clearly not conducive to the preservation of hemipelagic calcisphere dolostones (which are notably absent during these intervals of V and Zn enrichment), and thus may have been acidic. The absence of sulfur enrichments implies ferruginous, rather than fully euxinic conditions in the bottom water.

These anoxic intervals are punctuated by brief periods of apparently more hospitable conditions (2301–2307 mbs, 2324–2335 mbs), which lack enrichment in redox sensitive elements, and do contain calcispheric dolostones similar to those seen in the Middle Montney (i.e., Smithian substage). The onset of these non-restricted periods, both here and in the

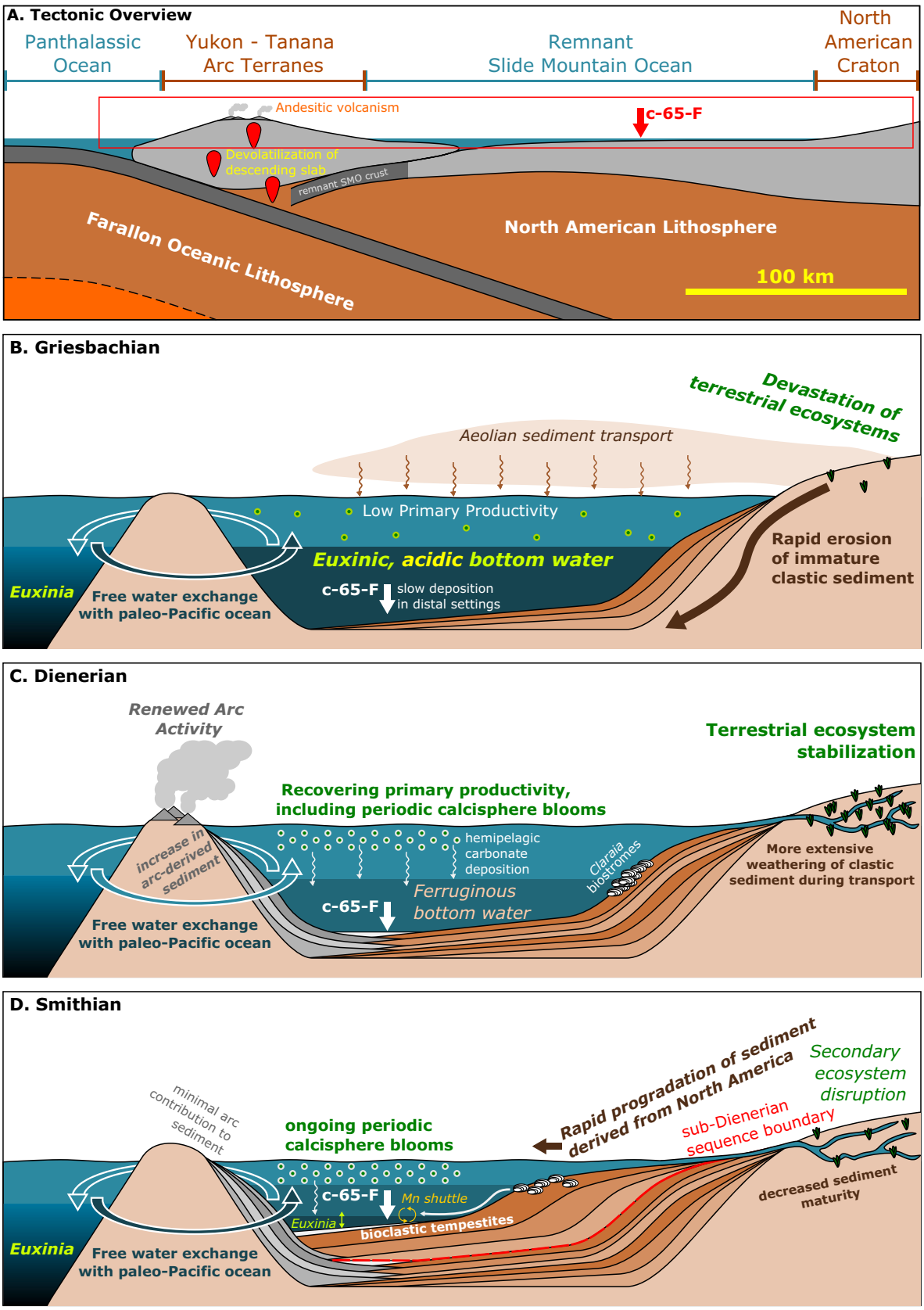

Fig. 7. Schematic plots of the Montney depositional environment. Panel A: Scaled tectonic overview of the western Pangaean margin in the Early Triassic, with the interpreted depositional location of Core c-65-F. Red box shows the area highlighted in subsequent panels of Figs. 8 and 9, which are not drawn to scale. Panel B: Schematic overview of the Montney depositional basin in the Greisbachian. Panel C: Schematic overview of the Montney depositional basin in the Dienerian (with similar conditions extending into the early Smithian). Panel D: Schematic overview of the Montney depositional basin in the Smithian. (For interpretation of the references to color in this figure legend, the reader is referred to the web version of this article.)

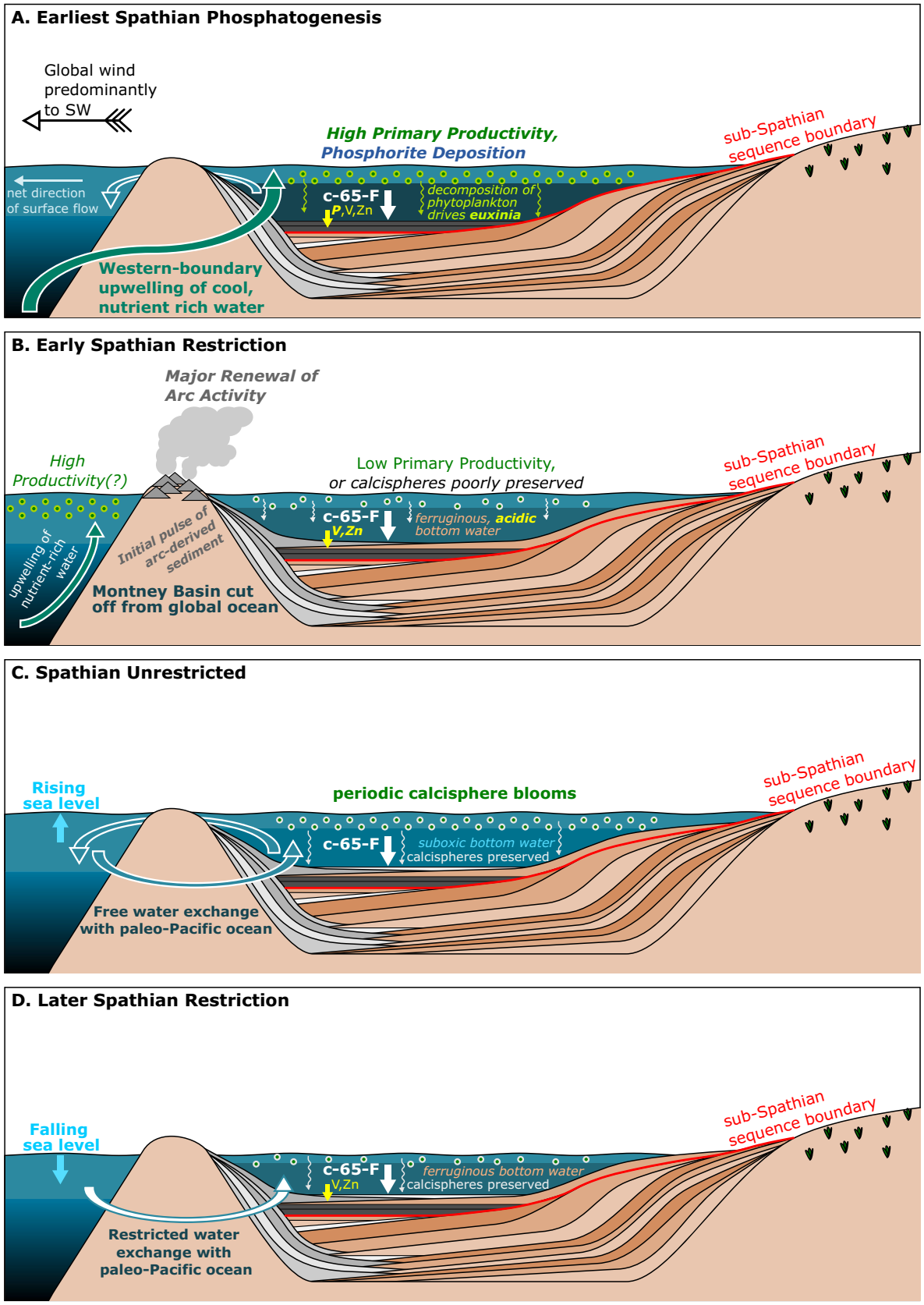

Fig. 8. Schematic plots of different Spathian modalities in the Montney depositional environment. Panel D: Upwelling and phosphatogenesis during the earliest Spathian, corresponding to green highlight in Figs. 4–6. Panel E: Intervals of intense restriction during the early Spathian, corresponding to darker blue highlights in Fig. 4–6. Panel F: Spathian intervals of open communication with the paleo-Pacific, not highlighted in Figs. 4–6. Panel G: Intervals of weak restriction in the later Spathian, highlighted in lighter blue in Figs. 4–6. (For interpretation of the references to color in this figure legend, the reader is referred to the web version of this article.)

upper Spathian (see below), in all cases coincide with recognized marine flooding surfaces, identified sedimentologically as transitions to fine-grained, bituminous siltstones representing deeper settings (Moslow et al., 2018; Zonneveld and Moslow, 2018). Each cycle likely coincides with one 100 kyr cycle in short eccentricity, suggesting a direct relationship with Milankovitch cycles and relative sea level (Shen, 2018).

Rising seas may have established shallow channels and spillways through the dissected Yukon-Tanana barrier, allowing for better connection between the Slide Mountain Ocean and the Panthalassic (Fig. 8C). In this relatively shallow basin, little change in sea level would be needed (likely on the order of 10 m or less), and the process may have been controlled by astronomical cycles. Cyclical variation can also be seen in Rb/(Rb + K) throughout the Spathian, (Fig. 4), and may reflect climatic influence on weathering intensity.

5.5. The uppermost Olenekian: upper Spathian substage and basal Anisian Stage

Episodes of apparent restriction and anoxia, as recognized by elevated V and Zn content and elevated PC 2 scores, continue into the later Spathian. At least three of these episodes can be discerned, from 2206–2238 mbs, 2251–2260 mbs and 2270–2301 mbs. As in the lower Spathian, at least some of these episodes seem to be terminated by flooding surfaces (Moslow et al., 2018; Zonneveld and Moslow, 2018), suggesting that rising sea level allowed water from the open Panthalassic Ocean to circulate freely into the basin across the Yukon-Tanana barrier.

Several lines of evidence suggest that these latter episodes of restriction may not have been as intense as those seen in the earlier Spathian. Absolute values of redox-sensitive metals during restricted intervals decrease throughout the Spathian (Fig. 5), as do scores for PC2 (Fig. 6). Interestingly, sulfur values (and the correlated PC3 scores) are consistently low and not correlated with other redox proxies during these episodes of restriction (Figs. 5,6), suggesting that conditions were ferruginous rather than euxinic. Unlike the lower Spathian restricted intervals, bottom water conditions during these later episodes do not seem to have precluded the preservation of calcisphere dolostones (identifiable as sharp shifts in PC1; Fig. 6), which coexist with enrichments in V and Zn (Fig. 8D). Like the lower Spathian, these later restricted intervals are punctuated by intervals of non-restriction (Fig. 8C), identifiable from 2192–2206 mbs, 2238–2251 mbs, and 2260–2270 mbs, all of which begin in facies immediately overlying interpreted flooding surfaces (Zonneveld and Moslow, 2018).

The transition from the Montney Formation to overlying Anisian units is clearly discernable in geochemical data. The sandy Sunset Prairie Formation (Furlong et al., 2018) can be recognized via an abrupt increase in Si content. Other geochemical proxies indicate immature sediment containing a mafic component, suggesting that these coarser sediments may have been sourced from the Yukon-Tanana terrane to the west rather than cratonic North America (Fig. 4). While PC2 is elevated, most lines of evidence (i.e., V, Zn, S, As) suggest deposition under increasingly oxic conditions, an inference consistent with the robust and diverse benthic macrofossil communities (bivalves, gastropods, brachiopods, echinoids and crinoids) and trace fossil assemblages observed in this interval of the core (Furlong et al., 2018; Moslow et al., 2018). In the overlying Phosphate Member of the Doig Formation, an increase in PC4 suggests high primary productivity, while an increase in PC3 suggests a return to euxinic conditions. This may reflect a more sustained resumption of coastal upwelling, similar to that seen in the earliest Spathian, as well as a return to more vigorous nutrient cycling in the Middle Triassic (Grasby et al., 2016, 2020).

5.6. Global implications of the Early Triassic geochemistry of the Montney Formation

In summary, the Lower-Middle Montney shows a clear tripartite structure, which likely reflects global oceanographic trends. The Griesbachian was an interval of rapid warming in the tropical ocean (Sun et al., 2012), coupled with expansion of oceanic anoxia (Lau et al., 2016; Zhang et al., 2018a, 2018b) and euxinia impinging into shallow marine settings (Grice et al., 2005; Hays et al., 2007). While sedimentation rates were low in the distal location of c-65-F, geochemical results suggest sediment was produced via the rapid erosion of the arid North American margin, consistent with studies indicating elevated Early Triassic weathering rates (Algeo and Twitchett, 2010; Algeo et al., 2011; Hermann et al., 2011). The Dienerian was an interval of cooling climate and incipient recovery, prior to a Smithian Thermal Maximum (Sun et al., 2012; Zhao et al., 2020; Du et al., 2022) that returned the environment to Griesbachian-like conditions. In contrast to other sections, no Smithian 'carbonate crisis' (Widmann et al., 2020) is seen in this setting, with carbonate deposition continuing throughout the Smithian. These patterns reinforce the conclusion that global-scale fluctuations in temperature and ocean circulation, driven by eruption of the Siberian Traps Large Igneous Province, controlled the tempo and dynamics of recovery in the Early Triassic on the largest scale (Wei et al., 2015).

In contrast, the Spathian interval is more dominated by local signals, reflecting the closure of the Slide Mountain Ocean and tectonics of the Yukon-Tanana arc. Globally, cooler conditions following the Smithian Thermal Maximum (Sun et al., 2012; Goudemand et al., 2019) led to an early Spathian excursion toward more oxic conditions in the eastern Panthalassic (Zhang et al., 2019a, 2019b) and broader global ocean (Zhao et al., 2020). The brief interval of phosphatogenesis in the lowermost Spathian is consistent with evidence for enhanced oceanic overturning circulation (Lyu et al., 2019; Song et al., 2019), though uplift of the Yukon-Tanana boundary likely pushed upwelling outboard of the Slide Mountain Ocean through most of the Spathian. The transition to the phosphatic Doig Formation may be related to a broader recovery from nutrient stress in the Panthalassic realm (Grasby et al., 2020; Du et al., 2023).

6. Conclusions

Extremely high-resolution geochemical datasets generated by ITRAX core scanning, when calibrated using conventional geochemical techniques, can provide insights into the depositional history of sedimentary units at an unprecedented level of detail. While not all elements yield useful signals, meaningful proxies for provenance, weathering, redox conditions and productivity can be identified. Principal components analysis can be a viable tool for extracting useful signals from multiple elements with different responses to XRF scanning and varying signal-to-noise ratios.

The distal Montney Formation was influenced by a complex interplay of global conditions and local tectonics and paleogeography. Redox conditions during deposition of the Lower and Middle Montney Formation (Griesbachian – Smithian) were dynamic, reflecting global climatic and oceanographic patterns. Predominantly ferruginous conditions were punctuated by episodes of euxinia in the Griesbachian and Smithian substages, with diminished euxinia in the Dienerian allowing for limited recovery of carbonate producers. By the Spathian substage, the Upper Montney depositional basin was primarily affected by local tectonic and oceanographic factors, and was episodically shielded from the global ocean by the Yukon-Tanana arc. This allowed for the development of basinal restriction, punctuated by short periods of relative oxygenation driven by small changes in sea level. Where evidence for euxinia is seen in this interval, it typically coincides with evidence for high productivity, reflecting the recovery of coastal upwelling.

CRediT authorship contribution statement

Shane D. Schoepfer: Writing – review & editing, Writing – original draft, Investigation, Conceptualization. **Charles M. Henderson:**

Writing – review & editing, Writing – original draft, Resources, Investigation, Funding acquisition, Conceptualization. **Thomas F. Moslow:** Investigation, Conceptualization. **Chen Shen:** Investigation, Conceptualization.

Declaration of competing interest

The authors declare that they have no known competing financial interests or personal relationships that could have appeared to influence the work reported in this paper.

Data availability

Data will be made available on request.

Acknowledgments

The authors would like to express their gratitude to Petronas Canada Ltd. (formerly Progress Energy Canada Ltd.), especially to Gerald Nyberg, Matt Adams, and Wayne Hovdebo, and Sasol Exploration and Production Ltd. for providing us with this dataset, generous postdoctoral support to SS and research support to CMH, and the permission to share these findings with the broader geologic community. CMH also acknowledges NSERC Discovery Grant support.

Appendix A. Supplementary data

Supplementary data to this article can be found online at https://doi.org/10.1016/j.palaeo.2024.112019.

References

Algeo, T.J., Liu, J., 2020. A re-assessment of elemental proxies for paleoredox analysis. Chem. Geol. 540, 119549.
Algeo, T.J., Twitchett, R.J., 2010. Anomalous Early Triassic sediment fluxes due to elevated weathering rates and their biological consequences. Geology 38 (11), 1023–1026.
Algeo, T.J., Chen, Z.Q., Fraiser, M.L., Twitchett, R.J., 2011. Terrestrial–marine teleconnections in the collapse and rebuilding of Early Triassic marine ecosystems. Palaeogeogr. Palaeoclimatol. Palaeoecol. 308 (1–2), 1–11.
Beauchamp, B., Baud, A., 2002. Growth and demise of Permian biogenic chert along northwest Pangea: evidence for end-Permian collapse of thermohaline circulation. Palaeogeogr. Palaeoclimatol. Palaeoecol. 184 (1–2), 37–63.
Beauchamp, B., Grasby, S.E., 2012. Permian lysocline shoaling and ocean acidification along NW Pangea led to carbonate eradication and chert expansion. Palaeogeogr. Palaeoclimatol. Palaeoecol. 350, 73–90.
Beranek, L.P., Mortensen, J.K., 2011. The timing and provenance record of the Late Permian Klondike orogeny in northwestern Canada and arc-continent collision along western North America. Tectonics 30 (5), TC5017.
Beranek, L.P., Mortensen, J.K., Orchard, M.J., Ullrich, T., 2010. Provenance of North American Triassic strata from west-central and southeastern Yukon: correlations with coeval strata in the Western Canada Sedimentary Basin and Canadian Arctic Islands. Can. J. Earth Sci. 47 (1), 53–73.
Brar, R.J., 2021. Sequence Biostratigraphy and Chronostratigraphy of the Lower Triassic Montney Formation, northeast British Columbia and west-central Alberta. Unpublished MSc thesis. University of Calgary, 117 pp.
Brumsack, H.J., 2006. The trace metal content of recent organic carbon-rich sediments: implications for Cretaceous black shale formation. Palaeogeogr. Palaeoclimatol. Palaeoecol. 232 (2–4), 344–361.
Calvert, S.E., Pedersen, T.F., 2007. Chapter fourteen elemental proxies for palaeoclimatic and palaeoceanographic variability in marine sediments: interpretation and application. Dev. Marine Geol. 1, 567–644.
Colpron, M., Nelson, J.L., 2009. A Palaeozoic Northwest Passage: Incursion of Caledonian, Baltican and Siberian terranes into eastern Panthalassa, and the early evolution of the North American Cordillera. Geol. Soc. Lond. Spec. Publ. 318 (1), 273–307.
Croudace, I.W., Rindby, A., Rothwell, R.G., 2006. ITRAX: description and evaluation of a new multi-function X-ray core scanner. Geol. Soc. Lond. Spec. Publ. 267 (1), 51–63.
Davies, G.R., Moslow, T.F., Sherwin, M.D., 1997. The Lower Triassic Montney Formation, west-central Alberta. Bull. Can. Petrol. Geol. 45 (4), 474–505.
Davies, G.R., Watson, N., Moslow, T.F., MacEachern, J.A., 2018. Regional subdivisions, sequences, correlations and facies relationships of the Lower Triassic Montney Formation, west-central Alberta to northeastern British Columbia, Canada—with emphasis on role of paleostructure. Bull. Can. Petrol. Geol. 66 (1), 23–92.
Du, Y., Song, H., Algeo, T.J., Song, H., Tian, L., Chu, D., Shi, W., Li, C., Tong, J., 2022. A massive magmatic degassing event drove the Late Smithian Thermal Maximum and Smithian–Spathian boundary mass extinction. Glob. Planet. Chang. 215, 103878.
Du, Y., Song, H., Grasby, S.E., Xing, T., Song, H., Tian, L., Chu, D., Wu, Y., Dal Corso, J., Algeo, T.J., Tong, J., 2023. Recovery from persistent nutrient-N limitation following the Permian–Triassic mass extinction. Earth Planet. Sci. Lett. 602, 117944.
Euzen, T., Moslow, T.F., Crombez, V., Rohais, S., 2018. Regional stratigraphic architecture of the Spathian deposits in western Canada—Implications for the Montney resource play. Bull. Can. Petrol. Geol. 66 (1), 175–192.
Furlong, C.M., Gingras, M.K., Moslow, T.F., Zonneveld, J.P., 2018. The Sunset Prairie Formation: designation of a new Middle Triassic formation between the Lower Triassic Montney Formation and Middle Triassic Doig Formation in the Western Canada Sedimentary Basin, northeast British Columbias. Bull. Can. Petrol. Geol. 66 (1), 193–214.
Goudemand, N., Romano, C., Leu, M., Bucher, H., Trotter, J.A., Williams, I.S., 2019. Dynamic interplay between climate and marine biodiversity upheavals during the Early Triassic Smithian-Spathian biotic crisis. Earth Sci. Rev. 195, 169–178.
Grasby, S.E., Beauchamp, B., Knies, J., 2016. Early Triassic productivity crises delayed recovery from world's worst mass extinction. Geology 44 (9), 779–782.
Grasby, S.E., Knies, J., Beauchamp, B., Bond, D.P., Wignall, P., Sun, Y., 2020. Global warming leads to Early Triassic nutrient stress across northern Pangea. GSA Bull. 132 (5–6), 943–954.
Grasby, S.E., Bond, D.P.G., Wignall, P.B., Yin, R., Strachan, L.J., Takahashi, S., 2021. Transient Permian-Triassic euxinia in the southern Panthalassa deep ocean. Geology. https://doi.org/10.1130/G48928.1.
Grice, K., Cao, C., Love, G.D., Böttcher, M.E., Twitchett, R.J., Grosjean, E., Summons, R. E., Turgeon, S.C., Dunning, W., Jin, Y., 2005. Photic zone euxinia during the Permian-Triassic superanoxic event. Science 307 (5710), 706–709.
Hammer, Ø., Harper, D.A., Ryan, P.D., 2001. PAST: Paleontological statistics software package for education and data analysis. Palaeontol. Electron. 4 (1), 9.
Hays, Lindsay E., Beatty, Tyler, Henderson, Charles M., Love, Gordon D., Summons, Roger E., 2007. Evidence for photic zone euxinia through the end-Permian mass extinction in the Panthalassic Ocean (Peace River Basin, Western Canada). Palaeoworld 16 (1), 39–50.
Helmke, P.A., Sparks, D.L., 1996. Lithium, sodium, potassium, rubidium, and cesium. In: Methods of Soil Analysis: Part 3 Chemical Methods, 5, pp. 551–574.
Henderson, C.M., Golding, M.L., Orchard, M.J., 2018. Conodont sequence biostratigraphy of the Lower Triassic Montney Formation. Bull. Can. Petrol. Geol. 66 (1), 7–22.
Hermann, E., Hochuli, P.A., Bucher, H., Brühwiler, T., Hautmann, M., Ware, D., Roohi, G., 2011. Terrestrial ecosystems on North Gondwana following the end-Permian mass extinction. Gondwana Res. 20 (2–3), 630–637.
Huang, Y., Tong, J., Fraiser, M.L., 2018. A Griesbachian (Early Triassic) mollusc fauna from the Sidazhai Section, Southwest China, with paleoecological insights on the proliferation of genus Claraia (Bivalvia). J. Earth Sci. 29 (4), 794–805.
Knies, J., Schönenberger, J., Zwingmann, H., van der Lelij, R., Smelror, M., Vullum, P.E., Brönner, M., Vogt, C., Fredin, O., Müller, A., Grasby, S.E., 2022. Continental weathering and recovery from ocean nutrient stress during the Early Triassic Biotic Crisis. Commun. Earth Environ. 3 (1), 161.
Lau, K.V., Maher, K., Altiner, D., Kelley, B.M., Kump, L.R., Lehrmann, D.J., Silva-Tamayo, J.C., Weaver, K.L., Yu, M., Payne, J.L., 2016. Marine anoxia and delayed Earth system recovery after the end-Permian extinction. Proc. Natl. Acad. Sci. 113 (9), 2360–2365.
Lindström, S., Bjerager, M., Alsen, P., Sanei, H., Bojesen-Koefoed, J., 2020. The Smithian–Spathian boundary in North Greenland: implications for extreme global climate changes. Geol. Mag. 157 (10), 1547–1567.
Löwemark, L., Bloemsma, M., Croudace, I., Daly, J.S., Edwards, R.J., Francus, P., Galloway, J.M., Gregory, B.R., Huang, J.J.S., Jones, A.F., Kylander, M., 2019. Practical guidelines and recent advances in the Itrax XRF core-scanning procedure. Quat. Int. 514, 16–29.
Lyons, T.W., Severmann, S., 2006. A critical look at iron paleoredox proxies: New insights from modern euxinic marine basins. Geochim. Cosmochim. Acta 70 (23), 5698–5722.
Lyu, Z., Zhang, L., Algeo, T.J., Zhao, L., Chen, Z.Q., Li, C., Ma, B., Ye, F., 2019. Global-ocean circulation changes during the Smithian–Spathian transition inferred from carbon-sulfur cycle records. Earth Sci. Rev. 195, 114–132.
McLennan, S.M., Hemming, S., McDaniel, D.K., Hanson, G.N., 1993. Geochemical approaches to sedimentation, provenance, and tectonics. Spec. Pap. Geol. Soc. Am. 21.
Meyer, K.M., Kump, L.R., Ridgwell, A., 2008. Biogeochemical controls on photic-zone euxinia during the end-Permian mass extinction. Geology 36 (9), 747–750.
Moslow, T.F., Davies, G.R., 1997. Turbidite reservoir facies in the Lower Triassic Montney Formation, west-central Alberta. Bull. Can. Petrol. Geol. 45 (4), 507–536.
Moslow, T.F., Adams, M.G., Terzuoli, A., Haverslew, B., 2017. Unconventional Reservoir Facies Characteristics of the Montney Formation Resource Play in the Western Canada Sedimentary Basin. Am. Assoc. Petrol. Geol. Search Discov. Article #11029, 18pp.
Moslow, T.F., Haverslew, B., Henderson, C.M., 2018. Sedimentary facies, petrology, reservoir characteristics, conodont biostratigraphy and sequence stratigraphic framework of a continuous (395m) full diameter core of the Lower Triassic Montney Fm, northeastern British Columbia. Bull. Can. Petrol. Geol. 66 (1), 259–287.
National Energy Board (NEB), 2013. The ultimate potential for unconventional petroleum from the Montney Formation of British Columbia and Alberta—Energy briefing note.
Nelson, J.L., Colpron, M., Piercey, S.J., Dusel-Bacon, C., Murphy, D.C., Roots, C.F., 2006. Paleozoic tectonic and metallogenetic evolution of pericratonic terranes in Yukon, northern British Columbia and eastern Alaska. In: Paleozoic Evolution and

Metallogeny of Pericratonic Terranes at the Ancient Pacific Margin of North America, Canadian and Alaskan Cordillera: Geological Association of Canada Special Paper, 45, pp. 323–360.
Nesbitt, H., Young, G.M., 1982. Early Proterozoic climates and plate motions inferred from major element chemistry of lutites. Nature 299 (5885), 715–717.
Rohais, S., Crombez, V., Euzen, T., Zonneveld, J.P., 2018. Subsidence dynamics of the Montney Formation (Early Triassic, Western Canada Sedimentary Basin): insights for its geodynamic setting and wider implications. Bull. Can. Petrol. Geol. 66 (1), 128–160.
Schoepfer, S.D., Henderson, C.M., 2022. Paleogeographic implications of open-marine anoxia in the Permian–Triassic Slide Mountain Ocean. SEPM Special Publication No. 113. In: Late Paleozoic and Early Mesozoic Tectonostratigraphy and Biostratigraphy of Western Pangea, pp. 205–225.
Schoepfer, S.D., Henderson, C.M., Garrison, G.H., Foriel, J., Ward, P.D., Selby, D., Hower, J.C., Algeo, T.J., Shen, Y., 2013. Termination of a continent-margin upwelling system at the Permian–Triassic boundary (Opal Creek, Alberta, Canada). Glob. Planet. Chang. 105, 21–35.
Schoepfer, S.D., Shen, J., Wei, H., Tyson, R.V., Ingall, E., Algeo, T.J., 2015. Total organic carbon, organic phosphorus, and biogenic barium fluxes as proxies for paleomarine productivity. Earth Sci. Rev. 149, 23–52.
Shaw, P.J., 2009. Multivariate Statistics for the Environmental Sciences. Wiley.
Shen, C., 2018. Astronomical tuning, astronomical forcing and environmental conditions of the Lower Triassic Montney Formation, northeastern British Columbia, Canada. Masters Thesis. University of Calgary, PRISM Repository, Graduate Program in Geology and Geophysics, 105pp.
Shen, J., Schoepfer, S.D., Feng, Q., Zhou, L., Yu, J., Song, H., Wei, H., Algeo, T.J., 2015. Marine productivity changes during the end-Permian crisis and Early Triassic recovery. Earth Sci. Rev. 149, 136–162.
Song, H., Du, Y., Algeo, T.J., Tong, J., Owens, J.D., Song, H., Tian, L., Qiu, H., Zhu, Y., Lyons, T.W., 2019. Cooling-driven oceanic anoxia across the Smithian/Spathian boundary (mid-Early Triassic). Earth Sci. Rev. 195, 133–146.
Song, H., Song, H., Tong, J., Gordon, G.W., Wignall, P.B., Tian, L., Zheng, W., Algeo, T.J., Liang, L., Bai, R., Wu, K., 2021. Conodont calcium isotopic evidence for multiple shelf acidification events during the Early Triassic. Chem. Geol. 562, 120038.
Sun, Y., Joachimski, M.M., Wignall, P.B., Yan, C., Chen, Y., Jiang, H., Wang, L., Lai, X., 2012. Lethally hot temperatures during the Early Triassic greenhouse. Science 338 (6105), 366–370.
Thomson, J., Croudace, I.W., Rothwell, R.G., 2006. A geochemical application of the ITRAX scanner to a sediment core containing eastern Mediterranean sapropel units. Geol. Soc. Lond. Spec. Publ. 267 (1), 65–77.
Tribovillard, N., 2020. Arsenic in marine sediments: how robust a redox proxy? Palaeogeogr. Palaeoclimatol. Palaeoecol. 550, 109745.
Tribovillard, N., Algeo, T.J., Lyons, T., Riboulleau, A., 2006. Trace metals as paleoredox and paleoproductivity proxies: an update. Chem. Geol. 232 (1–2), 12–32.
Wei, H., Shen, J., Schoepfer, S.D., Krystyn, L., Richoz, S., Algeo, T.J., 2015. Environmental controls on marine ecosystem recovery following mass extinctions, with an example from the Early Triassic. Earth Sci. Rev. 149, 108–135.
Widmann, P., Bucher, H., Leu, M., Vennemann, T., Bagherpour, B., Schneebeli-Hermann, E., Goudemand, N., Schaltegger, U., 2020. Dynamics of the largest carbon isotope excursion during the Early Triassic biotic recovery. Front. Earth Sci. 8, 196.
Wignall, P.B., Newton, R., 2003. Contrasting deep-water records from the Upper Permian and Lower Triassic of South Tibet and British Columbia: evidence for a diachronous mass extinction. Palaios 18 (2), 153–167.
Zhang, L., Zhao, L., Chen, Z.Q., Algeo, T.J., Li, Y., Cao, L., 2015. Amelioration of marine environments at the Smithian–Spathian boundary, Early Triassic. Biogeosciences 12 (5), 1597–1613.
Zhang, G., Zhang, X., Hu, D., Li, D., Algeo, T.J., Farquhar, J., Henderson, C.M., Qin, L., Shen, M., Shen, D., Schoepfer, S.D., Chen, K., Shen, Y., 2017. Redox chemistry changes in the Panthalassic Ocean linked to the end-Permian mass extinction and delayed Early Triassic biotic recovery. Proc. Natl. Acad. Sci. 114 (8), 1806–1810.
Zhang, F., Algeo, T.J., Romaniello, S.J., Cui, Y., Zhao, L., Chen, Z.Q., Anbar, A.D., 2018a. Congruent Permian-Triassic δ238U records at Panthalassic and Tethyan sites: Confirmation of global-oceanic anoxia and validation of the U-isotope paleoredox proxy. Geology 46 (4), 327–330.
Zhang, F., Romaniello, S.J., Algeo, T.J., Lau, K.V., Clapham, M.E., Richoz, S., Herrmann, A.D., Smith, H., Horacek, M., Anbar, A.D., 2018b. Multiple episodes of extensive marine anoxia linked to global warming and continental weathering following the latest Permian mass extinction. Sci. Adv. 4 (4), e1602921.
Zhang, F., Algeo, T.J., Cui, Y., Shen, J., Song, H., Sano, H., Rowe, H.D., Anbar, A.D., 2019a. Global-ocean redox variations across the Smithian-Spathian boundary linked to concurrent climatic and biotic changes. Earth Sci. Rev. 195, 147–168.
Zhang, L., Orchard, M.J., Brayard, A., Algeo, T.J., Zhao, L., Chen, Z.Q., Lyu, Z., 2019b. The Smithian/Spathian boundary (late Early Triassic): a review of ammonoid, conodont, and carbon-isotopic criteria. Earth Sci. Rev. 195, 7–36.
Zhao, H., Dahl, T.W., Chen, Z.Q., Algeo, T.J., Zhang, L., Liu, Y., Hu, Z., Hu, Z., 2020. Anomalous marine calcium cycle linked to carbonate factory change after the Smithian Thermal Maximum (Early Triassic). Earth Sci. Rev. 211, 103418.
Zonneveld, J.P., Moslow, T.F., 2018. Palaeogeographic setting, lithostratigraphy, and sedimentary framework of the Lower Triassic Montney Formation of western Alberta and northeastern British Columbia. Bull. Can. Petrol. Geol. 66 (1), 93–127.
Zonneveld, J.P., Beatty, T.W., MacNaughton, R.B., Pemberton, S.G., Utting, J., Henderson, C.M., 2010. Sedimentology and ichnology of the Lower Triassic Montney Formation in the Pedigree-Ring/Border-Kahntah River area, northwestern Alberta and northeastern British Columbia. Bull. Can. Petrol. Geol. 58 (2), 115–140.